

A Minimal Self-organisation model of the Golgi Apparatus

Quentin Vagne^{a,1}, Jean-Patrick Vrel^{b,1}, Pierre Sens^b

*For correspondence:

pierre.sens@curie.fr (PS)

¹These authors contributed equally
to this work

^aCenter for Systems Biology Dresden, Max Planck Institute of Molecular Cell Biology and Genetics, 01307 Dresden, Germany; ^bLaboratoire Physico Chimie Curie, Institut Curie, PSL Research University, CNRS UMR168, 75005, Paris, France

Abstract The design principles dictating the spatio-temporal organisation of eukaryotic cells, and in particular the mechanisms controlling the self-organisation and dynamics of membrane-bound organelles such as the Golgi apparatus, remain elusive. Although this organelle was discovered 120 years ago, such basic questions as whether vesicular transport through the Golgi occurs in an anterograde (from entry to exit) or retrograde fashion are still strongly debated. Here, we address these issues by studying a quantitative model of organelle dynamics that includes: *de-novo* compartment generation, inter-compartment vesicular exchange, and biochemical conversion of membrane components. We show that anterograde or retrograde vesicular transports are asymptotic behaviors of a much richer dynamical system. Indeed, the structure and composition of cellular compartments and the directionality of vesicular exchange are intimately linked. They are emergent properties that can be tuned by varying the relative rates of vesicle budding, fusion and biochemical conversion.

Introduction

The Golgi apparatus is an intracellular organelle at the crossroad of the secretory, lysosomal and endocytic pathways (*Heald and Cohen-Fix, 2014*). One of its most documented functions is the sorting and processing of many proteins synthesized by eukaryotic cells (*Lippincott-Schwartz et al., 2000*). Proteins translated in the endoplasmic reticulum (ER) are addressed to the Golgi, where they undergo post-translational maturation and sorting, before being exported to their final destination. The Golgi itself is composed of distinct sub-compartments, called cisternae, of different biochemical identities (*Stanley, 2011*). From the ER, cargo-proteins successively reside in cisternae of the *cis*, *medial* and *trans*-identities, after which they exit the Golgi via the *trans*-Golgi network (TGN). In some organisms such as the yeast *Saccharomyces cerevisiae*, cisternae are dispersed throughout the cell (*Suda Yasuyuki and Nakano Akihiko, 2011*) and each cisterna undergoes maturation from a *cis* to a *trans*-identity (*Losev et al., 2006; Matsuura-Tokita et al., 2006*). In most other eukaryotes, cisternae are stacked in a polarized fashion, with cargo-proteins entering via the *cis*-face and exiting via the *trans*-face (*Boncompain and Perez, 2013*). This polarity is robustly conserved over time, despite cisternae constantly exchanging vesicles with each other, the ER and the TGN (*Lippincott-Schwartz et al., 2000*). Pharmacological treatments that alter the structure and stacking of Golgi compartments in mammalian cells affect the processing of certain proteins, and in particular glycosylation (*Hu et al., 2005; Shen et al., 2007; Xiang et al., 2013; Bekier et al., 2017*).

The highly dynamical nature and compact structure of a stacked Golgi makes it difficult to determine how cargo-proteins are transported in an anterograde fashion from the *cis* to *trans*-side of the stack and how this transport is coupled to processing. Several models have been proposed to explain the transport dynamics of Golgi cargo (See sketch in Fig.1 A). They mostly belong to

43 two classes: one involving stable compartments exchanging components through fusion-based
44 mechanisms and one involving transient compartments undergoing *en-block* maturation and in
45 which fusion mechanisms are dispensable for cargo transport. Historically (**Malhotra and Mayor, 2006**),
46 the "Vesicular transport" model postulated that cisternae have fixed identities and cargo
47 progresses from one cisterna to the next via anterograde vesicular transport, while the "Cisternal
48 Maturation" model postulated that cisternae themselves undergo maturation from the *cis* to the
49 *trans*-identity and physically move through the stack, while Golgi resident proteins remain in the
50 stack by moving toward the *cis*-face by retrograde vesicular transport. Several extensions of these
51 two models have been proposed, including cisternal maturation with tubular connections (**Trucco et al., 2004; Rizzo et al., 2013**), rapid partitioning within Golgi cisternae between processing and
52 exporting sub-compartments (**Patterson et al., 2008**), or the cisternal progenitor model (**Pfeffer, 2010**),
53 in which stable cisternae exchange material by the fusion and fission of sub-compartments
54 defined by their composition of Rab GTPases, which evolve over time through exchange with the
55 cytosol. The strengths and weaknesses of these different models are nicely reviewed in (**Glick and Luini, 2011**). Variations of these models, such as the "rim progression" model also exist (**Lavieu et al., 2013**). It is noteworthy that these models do not provide a quantitative analysis of the generation
56 and maintenance of Golgi compartments, nor do they attempt to relate the Golgi structure (number
57 and size of compartments) and transport dynamics. Therefore, much remains unknown regarding
58 the mechanisms that dictate the organisation and dynamics of the Golgi.

59 Although there is a large diversity in Golgi structures and dynamics among different species,
60 the physiological function of the organelle as a sorting and processing hub is common to all
61 species, suggesting that important mechanisms controlling Golgi dynamics are conserved. Works in
62 evolutionary biology and biophysics have attempted to describe these mechanisms (**Klute et al., 2011; Sens and Rao, 2013**). Different classes of mathematical models have been proposed, from
63 models of vesicle budding and fusion based on rate equations (**Binder et al., 2009; Ispolatov and Müsch, 2013; Mukherji and O'Shea, 2014**) - some specifically including space (**Sachdeva et al., 2016**),
64 to continuous, discrete and stochastic models of protein sorting in the Golgi (**Gong et al., 2010; Vagne and Sens, 2018b**) and computer simulations based on membrane mechanics (**Tachikawa and Mochizuki, 2017**). To account for the ability of the Golgi to reassemble after mitosis (**Wei and Seemann, 2017**), many of these studies have sought to describe the Golgi as a self-organized system
65 (**Binder et al., 2009; Kühnle et al., 2010**). However, the manner in which the kinetics of the Golgi
66 two main functions (namely the transport and biochemical conversion of its components) interplay
67 with one another to yield a robust steady-state has so far received much less attention (**Sachdeva et al., 2016; Vagne and Sens, 2018b**).

68 Most existing models discuss transport through a pre-existing compartmentalised Golgi structure.
69 The main goal of our model is to explain how this compartmentalised structure and the flux
70 within it can spontaneously emerge through self-organisation. We propose here a model in which
71 both Golgi self-organisation and vesicular transport are solely directed by (local) molecular interac-
72 tions resulting in composition-dependent budding and fusion. In particular, we neglect the spatial
73 structure of the Golgi, and assume that any two components of the system can interact with one
74 another (see the Discussion section for the relevance of this approximation). Thus, the directionality
75 of vesicular transport is an emergent property of the self-organisation process that co-evolves with
76 the size and number of Golgi sub-compartments, rather than being fixed by arbitrary rules. This
77 approach brings new conceptual insights that highlight the link between the large-scale steady-state
78 organisation of the Golgi, the directionality of vesicular transport, and the kinetics of individual
79 processes at the molecular scale. We show that a wide variety of organelle phenotypes can be ob-
80 served upon varying the rates of the local processes. In particular, our model uncovers a correlation
81 between the size and composition (purity) of Golgi sub-compartments. Besides, it emphasizes that
82 composition-dependent exchange between compartments yields complex vesicular flux patterns
83 that are neither purely anterograde (as in the "vesicular transport" model) nor purely retrograde (as
84 in the "cisternal maturation" model).

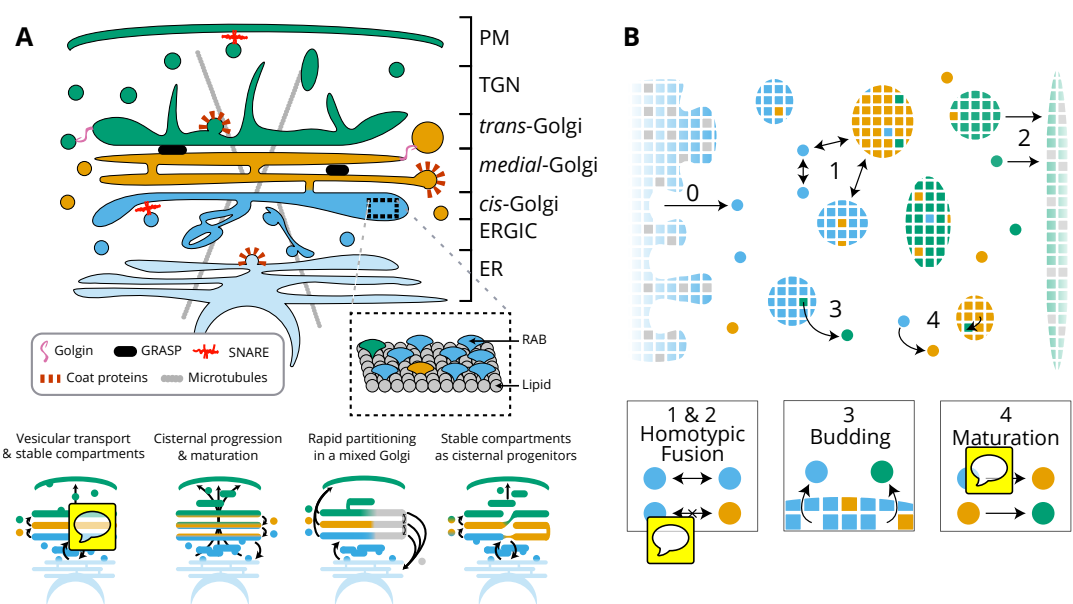


Figure 1. Model of golgi structure and transport (A) Top: classical representation of the structure of the Golgi, showing some of the important protein actors. The three main membrane identities are shown in different colors (*cis*: blue, *medial*: orange, *trans*: green): ER=Endoplasmic Reticulum, ERGIC= ER-Golgi intermediate Compartment, TGN=Trans-Golgi-Network, PM=Plasma Membrane. Bottom: Sketches of the four main models of Golgi transport (see text). (B) Our quantitative model of Golgi self-organisation. The left boundary is the ER, composed of a *cis*-membrane identity, and the right boundary is the TGN, composed of a *trans*-membrane identity. Golgi compartments self-organise via three stochastic mechanisms: **Fusion**: (1) All compartments can aggregate using homotypic fusion mechanisms: the fusion rate is higher between compartment of similar identities. (2) Each compartment can exit the system by fusing homotypically with the boundaries. **Budding**: (3) Each compartment larger than a vesicle can create a vesicle by losing a patch of membrane. **Biochemical conversion**: (4) Each patch of membrane undergoes a conversion from a *cis* to a *trans*-identity. New *cis*-vesicles (0) bud from the ER at a constant rate. In the sketch, the boundaries also contain neutral (gray) membrane species that dilute their identity (impact of this dilution in Appendix App.7, page p.39).

Model

The model, shown in Fig.1 and fully described in the Appendix App.1, is a coarse-grained representation of the Golgi Apparatus. The system is discretised at the scale of small vesicles, which define the unit size of the system. Vesicles can fuse together or with existing compartments to form larger compartments and can bud from compartments. Compartments consist of a number of membrane patches (of size unity) with distinct identities. The biochemical identity of a membrane patch is defined in a very broad sense by its composition in lipids and proteins that influence its interaction with other patches, such as Rab GTPases (Grosshans *et al.*, 2006) or fusion proteins such as SNAREs (Cai *et al.*, 2007). Consistently with the three main biochemical identities reported for Golgi membranes (Day *et al.*, 2013), vesicles and membrane patches are of either *cis*, *medial* or *trans*-identity, and can undergo irreversible biochemical conversion from the *cis* to the *trans*-identity. The system is fed by a constant influx J of *cis* vesicles coming from the ER, and vesicles and compartments can fuse homotypically with the ER (itself of *cis* identity) and the TGN (of *trans* identity).

Compartments are defined by their size n (a number of patches) and their composition, the fractions ϕ_i (with $i = \text{cis}, \text{medial}, \text{trans}$) of patches of the three different identities composing it. These quantities are dynamically controlled by three, composition dependent, microscopic mechanisms – budding, fusion and biochemical conversion – as described below.

- **Fusion:** Homotypic fusion – the higher probability of fusion between compartments of similar identities – is a feature of cellular organelles in general (Antonin *et al.*, 2000) and the Golgi apparatus in particular (Pfeffer, 2010; Bhave *et al.*, 2014). This is controlled here by a fusion

152 Codes used for the simulation can be found on the UMR168 Curie website, section
153 team-sens/software. [Click to access](#)

114 rate between compartments proportional to the probability that they present the same
115 identity at the contact site. The total fusion rate for two compartments (*a*) and (*b*) with
116 composition $\phi_i^{(a)}$ and $\phi_i^{(b)}$ for each identity *i* (with *i* equals *cis*, *medial* and *trans*) is then:

$$K_f \times \sum_i \phi_i^{(a)} \phi_i^{(b)} \quad (1)$$

117 where K_f is the fusion rate between two identical compartments. Fusion with the boundaries
118 follow the same rules, with the ER containing a fraction α_{ER} of *cis* patches and the TGN a fraction
119 α_{TGN} of *trans* patches. Numerical results described in the main paper are for $\alpha_{ER} = \alpha_{TGN} = 1$,
120 and the role of  composition of the boundaries is discussed in the App.7.

- 121 • **Budding:** Budding is the emission of a vesicle from a larger compartment. Composition-
122 dependent vesicular budding is an important sorting mechanism in cellular traffic (*Bonifacino*
123 and *Glick*, 2004). Owing to the high specificity of the budding machinery, each vesicle is
124 assumed to be composed of a single membrane identity. The budding flux for any components
125 *i* (equals *cis*, *medial* or *trans*) present in a compartment is assumed not to depend on the
126 number $n_i = n\phi_i$ of patches of identity *i*, but on the total size of the  compartment:

$$J_{b,i} = K_b \times n. \quad (2)$$

127 This budding kinetics corresponds to the saturated regime of a Michaelis-Menten reaction
128 kinetics, and is appropriate to the case where budding actors (e.g. coat proteins) bind non-
129 specifically to the membrane of the compartment and find their budding partners (a patch
130 of a particular identity) by  diffusion (*Vagne and Sens*, 2018b). An alternative budding scheme
131 where the budding flux is linear with the number of patches of a given identity ($J_{b,i} = K_b n_i$) is
132 discussed in App.8 on p.41 

- 133 • **Biochemical conversion:** Each  membrane patch is assumed to undergo stochastic biochemical
134 conversion from a *cis* to a *medial* to a *trans* identity. This local mechanism of identity
135 conversion is motivated by the Rab cascade,  during which the membrane identity evolves
136 over time through molecular exchange with the cytosol, as was observed in endosomes (*Rink*
137 et al., 2005) and in the Golgi of Yeast (*Losev* et al., 2006; *Matsuura-Tokita* et al., 2006). The
138 Rab conversion mechanism has not been demonstrated in mammalian Golgi, but is thought
139 to be universally important for the specificity of membrane trafficking (*Grosshans* et al., 2006),
140 and many of the proteins involved in the Yeast Rab cascade are conserved in mammalian cells
141 (*Klute* et al., 2011). Rab conversion is at the basis of the cisternal progenitor model (*Pfeffer*,
142 2010), and it is thus of fundamental importance to understand its potential implication on
143 Golgi structure and dynamics with the use of a quantitative model. We stress that our model
144 of biochemical conversion is not limited to Rab GTPases, but can also correspond to the modi-
145 fication of lipid components by enzymes in the Golgi (*McDermott* and *Mousley*, 2016). This
146 is a local mechanism of identity conversion distinct from the maturation of entire comp-
147 artments, which is also affected by the dynamics of budding and fusion. To limit the number of
148 parameters, the biochemical conversion rate K_m is the same for the two reactions (*cis*→*medial*
149 and *medial*→*trans*) and is independent of the concentration. Introducing cooperativity in the
150 conversion process is expected to increase the robustness of the self-organisation process
151 (*Vagne and Sens*, 2018a).

152 In its simplest form, our model contains only four parameters: the rates of injection, fusion,
153 budding, and biochemical  conversion (J , K_f , K_b , K_m). By normalizing time with the fusion rate,
154 we are left with three parameters: $j = J/K_f$, $k_b = K_b/K_f$ and $k_m = K_m/K_f$. The dynamics of the

157 system is entirely governed by these stochastic transition rates, and can be simulated exactly using
158 a Gillespie algorithm (**Gillespie, 1977**), described in App.1.

159 Results

160 Mean-field description of the system.

161 The complexity of the system prohibits rigorous analytical calculation. Nevertheless, analytical
162 results can be obtained for a number of interesting quantities in certain asymptotic regimes where
163 simplifying assumptions can be made. We present below some of these derivations.

164 De-novo formation and steady-state composition in the well-sorted limit

165 The composition of the system at steady-state is difficult to compute due to the fact that the exit of
166 components from the system, through fusion with the boundaries, depends on the composition of
167 the exiting compartments, which cannot be derived analytically in the general case. This calculation
168 becomes straightforward if the system is well sorted and all compartments are pure. As explained
169 below, this corresponds to the limit of high budding rate: $k_b \gg k_m$. In the well-sorted limit, only
170 *cis* components exit through the *cis* boundary and only *trans* components exit through the *trans*
171 boundary, and mean-field equations can be derived for the total amount N_{cis} , N_{medial} and N_{trans} of
172 each species:

$$\frac{\partial N_{cis}}{\partial t} = j - N_{cis}(\alpha_{ER} + k_m), \quad \frac{\partial N_{medial}}{\partial t} = k_m(N_{cis} - N_{medial}), \quad \frac{\partial N_{trans}}{\partial t} = k_m N_{medial} - \alpha_{TGN} N_{trans} \quad (3)$$

173 With j the injection rate of new *cis*-vesicles in the system and k_m the biochemical conversion rates,
174 both normalized by the fusion rate, and α_{ER} (α_{TGN}) is the fraction of *cis* (*trans*) species promoting
175 homotypic fusions with Golgi components in the ER (TGN).

176 At steady-state, the total amounts of *cis*, *medial* and *trans*-species are fixed by the balance between
177 influx, exchange, biochemical conversion and exit:

$$N_{cis} = N_{medial} = \frac{j}{\alpha_{ER} + k_m}, \quad N_{trans} = \frac{k_m}{\alpha_{TGN}} \frac{j}{\alpha_{ER} + k_m} \quad (4)$$

178 To estimate the typical size of compartments, we assume that for each species, a single large
179 compartment of size n interacts through budding and fusion with a number n_v of vesicles of the
180 same identity (so that $N = n + n_v$). The compartments size for each species then satisfies:

$$\frac{\partial n}{\partial t} = n_v - k_b n \xrightarrow{\text{steady state}} n = \frac{N}{1 + k_b} \quad (5)$$

To limit the number of parameters, we fix the average system's size $N = N_{cis} + N_{medial} + N_{trans}$ to a set value $N = 300$ in the main text, which is suitable for Golgi ministacks whose total area is of the order of $1\mu\text{m}^2$ (the area of a mammalian Golgi ribbon is much larger) (**Yelinek et al., 2009**), corresponding to about a few hundreds of vesicles of diameter $\sim 10 - 50\text{nm}$. This is obtained by adjusting the influx to the variation of the other parameters according to:

$$j = \frac{N (\alpha_{ER} + k_m) \alpha_{TGN}}{2\alpha_{TGN} + k_m} \quad (6)$$

181 We show in App.1 Fig.1 that the overall structure of the phase diagrams for the compartments size
182 and composition is robust upon variation of the average system's size.

183 The de-novo formation of the system can be approached with Eq.3. Starting with an empty
184 system with an influx $J (= K_f j)$ of *cis* vesicles, the system grows stochastically to reach the steady-
185 state size after a time of order $1/K_f$. The evolution of the size of the system with time obtained
186 from numerical simulations, shown in App.4, Fig.1 for different sets of parameters, agrees with Eq.3.
187 At steady-state, the influx of vesicles is balanced by an outflux of material. The exit kinetics can be
188 quantified by looking at the fate of a pulse of cargo released from the ER at a given time. App.4
189 Fig.2 shows that the exit kinetics is exponential, in agreement with results of FRAP (**Patterson et al.,**
190 **2008**) or pulse-chase (**Boncompain et al., 2012**) experiments.

191 Although Eq.6 is only valid in the well-sorted limit, it permits a satisfactory control of the average
192 system size over the entire range of parameters, with only a 10% variation for small budding rates
193 (App.5, Fig.1A). At steady-state, the system size exhibits stochastic fluctuations around the mean
194 value that depend on the parameters (App.5, Fig.1A). The large fluctuation (about 30%) for low
195 budding rate k_b stem from the fact that compartments are large and transient, as explained below.

196 **Compartment size and composition in the maturation-dominated regime.**
197 For low values of the budding rate k_b , compartments do not shed vesicles and evolve in time
198 independently of one another in a way dictated by a balance between fusion-mediated growth
199 and **biochemical maturation**. Their size and composition can be approximatively calculated by
200 assuming that compartments grow in size by fusion from a constant pool of vesicles containing the
201 same number n_v of vesicle for all three identities. Calling $n_{cis}(t)$, $n_{medial}(t)$ and $n_{trans}(t)$ the amount of
202 components of the three identities in a given compartment of total size $n = n_{cis} + n_{medial} + n_{trans}$, and
203 neglecting vesicle budding, the mean-field equations satisfied by these quantities are:

$$\partial_t n_{cis} = n_v \frac{n_{cis}}{n} - k_m n_{cis}, \quad \partial_t n_{medial} = n_v \frac{n_{medial}}{n} + k_m (n_{cis} - n_{medial}), \quad \partial_t n_{trans} = n_v \frac{n_{trans}}{n} + k_m n_{medial}. \quad (7)$$

Starting with a vesicle of *cis* identity for $t = 0$: $n_{cis}(0) = 1$, $n_{medial}(0) = n_{trans}(0) = 0$, the compartment size evolves linearly with time: $n(t) = 1 + n_v t$, and the composition of each species satisfies:

$$\begin{aligned} n_{cis}(t) &= (1 + n_v t) e^{-k_m t} \\ n_{medial}(t) &= (1 + n_v t) k_m t e^{-k_m t} \\ n_{trans}(t) &= (1 + n_v t) (1 - (1 + k_m t) e^{-k_m t}) \end{aligned} \quad (8)$$

204 The fraction of each species in the compartment is thus independent on n_v , and reads:

$$\phi_{cis}(t) = e^{-k_m t}, \quad \phi_{medial}(t) = k_m t e^{-k_m t}, \quad \phi_{trans}(t) = (1 - (1 + k_m t) e^{-k_m t}). \quad (9)$$

205 These results show that in this regime, a given compartment smoothly evolves from a mostly *cis*
206 to a mostly *trans* identity over a typical time $1/K_m$. The maximum amount of medial identity is
207 obtain for $k_m t = 1$ and is $\phi_{medial} = 1/e \approx 0.37$. Therefore, the mechanism does not lead to pure *medial*
208 compartments. These analytical results are confirmed by the full numerical solution of the system
209 in the low budding rate regime shown in App.5, p.34 and discussed in detail below.

210 **Steady-state organisation**

211 The steady-state organisation and dynamics of the system is described in terms of the average
212 size and purity of compartments (introduced here and detailed in the App.2). The stationary size
213 distribution of compartments is a decreasing function of the compartment size, which typically
214 shows a power law decay at small size, with an exponential cut-off at large size (Fig.2A). This
215 is expected for a non-equilibrium steady-state controlled by scission and aggregation (*Turner*
216 *et al., 2005*) and means that there exist many small compartments and very few large ones. The
217 typical compartment's size is defined as the ratio of the second over the first moments of the size
218 distribution. This corresponds to a size close to half the size of the exponential cut-off (see App.2)
219 beyond which it is unlikely to find a compartment (*Vagne et al., 2015*).

220 The typical compartment size varies with parameters as shown in Fig.2B. Increasing the **ratio of**
221 **budding to fusion rate** k_b , **decreases the compartment size** (*Turner et al., 2005*). The size depends on
222 the biochemical conversion rate k_m in a non-monotonic manner: for a given budding rate, the size
223 is smallest for intermediate values of the biochemical conversion rate ($k_m \approx 1$). The conversion rate
224 controls the composition of the compartment and hence their fusion probability. This dependency
225 is well explained by the simple analytical model discussed above (Eqs. 3,4) that approximates the
226 system by three pure compartments interacting with a pool of vesicles (solid lines in Fig.2B)>

227 The purity of a given compartment is defined as the (normalized) Euclidean distance of the
228 composition of the compartment (the fractions ϕ_i in the different *i*-identities, $i = cis, medial$ and

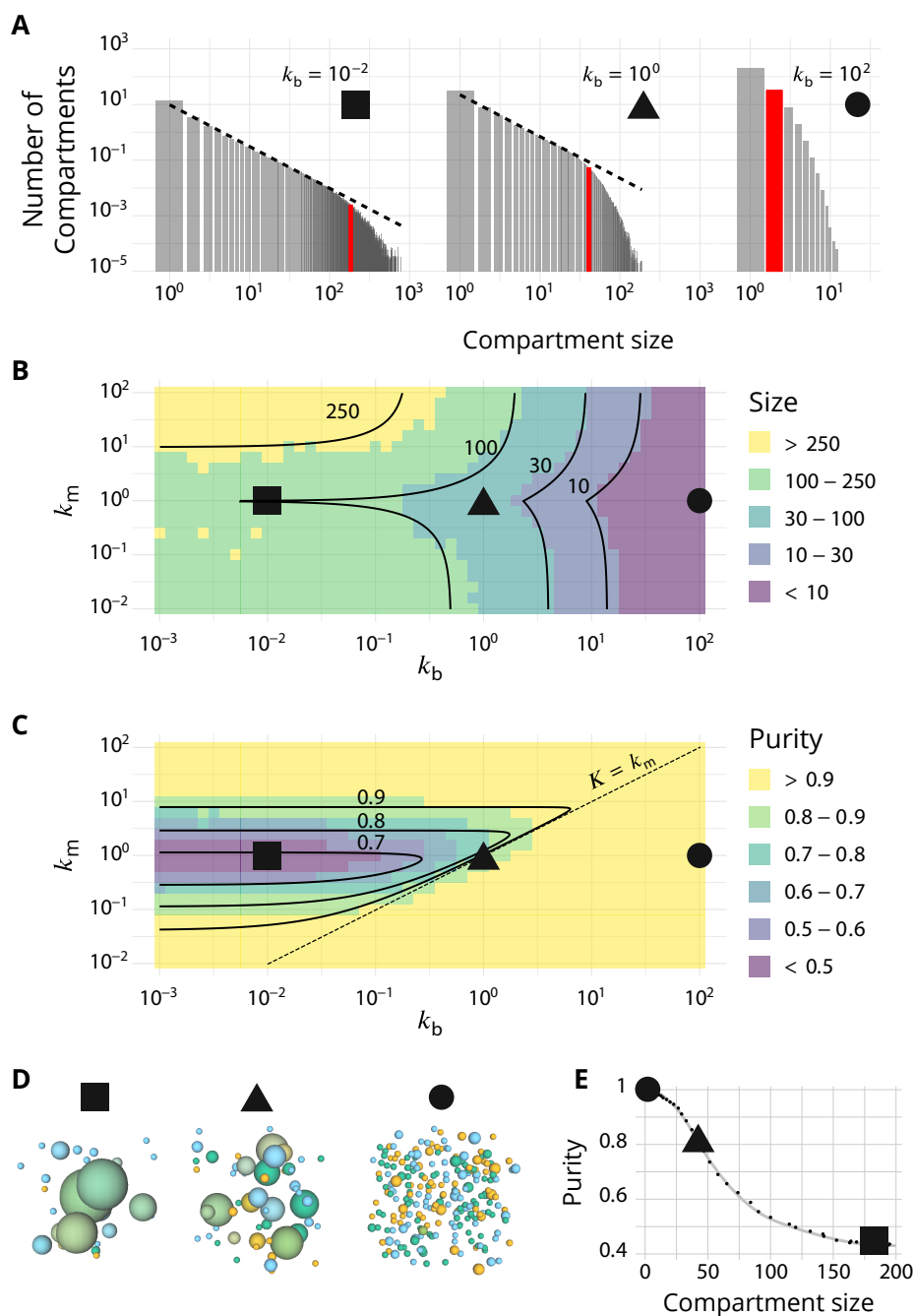


Figure 2. Steady-state of the self-organized model of Golgi apparatus. (A) Size distribution of compartments for a biochemical conversion rate $k_m = 1$ and different values of the budding rate k_b . The red bar shows the characteristic compartment size. (B) Phase diagram of the size of the compartments as the function of k_b and k_m . Black lines: theoretical prediction (Eqs.4,6) (C) Phase diagram of the purity of the system as a function of k_b and k_m . Dashed line is $k_m = k_b$, black lines are a theoretical prediction (see App.3, p.28). (D) System snapshots for $k_m = 1$ showing the *mixed regime* (square - $k_b = 10^{-2}$), the *sorted regime* (triangle - $k_b = 1$), and the *vesicular regime* (circle - $k_b = 10^2$) - see text. (E) Average compartment purity as a function of their average size, obtained by varying the budding rate k_b for $k_m = 1$ (black dots: simulation results - gray line: guide for the eyes). For all panels, $\alpha_{ER} = \alpha_{TGN} = 1$. See also App.5, p.34 for further characterizations of the steady-state organisation, App.7, p.39 for the role of composition of the exit compartment, and App.8, p.41 for results with alternative budding and fusion kinetics.

229 *trans*) from a perfectly mixed composition. $P = 0, 1/2, 1$ correspond respectively to compartments
230 that contain the same amount of the three identities, the same amount of two identities, and a single
231 identity (App.2, page p.25). The purity of the system is the average purity of each compartment
232 weighted by its size, ignoring vesicles. The dependency of the average purity with the parameters
233 is shown in Fig.2C. As for the size of the compartments, it is non-monotonic in the biochemical
234 conversion rate, and regions of lowest purity are found for intermediate biochemical conversion
235 rates $k_m \approx 1$, when all three identities are in equal amount. The purity increases with the budding
236 rate k_b in a sigmoidal fashion (see also Fig.3 A). This can be understood by analyzing the processes
237 involved in mixing and sorting of different identities. In a first approximation, mixing occurs by
238 biochemical conversion and sorting occurs by budding of contaminating species, suggesting a
239 **transitions from low to high purity when the budding rate reaches the biochemical conversion**
240 rate ($k_b \approx k_m$). A “purity transition” is indeed observed in an intermediate range of biochemical
241 conversion rates ($0.1 < k_m < 10$, see Fig.2C). It is most pronounced for $k_m \approx 1$. Beyond this range,
242 the system is dominated by one identity and compartments are always pure. The purity variation
243 can be qualitatively reproduced by an analytical model (App.3) that accounts for the competition
244 between biochemical conversion and budding, but also includes fusion between compartments
245 and with the exits (solid lines in Fig.2C.).

246 In summary, three types of organisation can be found, mostly controlled by the ratio of budding
247 over fusion rate k_b : a *mixed regime* at low k_b , where compartments are large and contain a mixture
248 of identities, a *vesicular regime* at high k_b , where compartments are made of only a few vesicles and
249 are very pure, and a *sorted regime* for intermediate values of k_b , where compartments are both
250 rather large, and rather pure. Snapshots of these three steady-states are shown in Fig.2D. The
251 relationship between average size and average purity of compartments is shown in Fig.2E. The
252 existence of a well-defined intermediate regime with large sorted compartments is promoted by
253 our assumption of “saturated budding” where the budding flux of any identity only depends on
254 the compartment size (Eq.2). If the budding flux is linear with the number of patches of a given
255 identity, the purity transition occurs for larger values of the budding rate k_b , where compartments
256 are smaller (see App.8, p.41).

257 **Vesicular Transport**

258 Vesicular exchange between compartments is quantified by following the dynamics over time of
259 passive cargo injected from the ER. Each cargo in a compartment of size n has a probability $1/n$ to
260 join a vesicle budding from this compartment. When this vesicle fuses with another compartment
261 or a boundary, the composition difference $\Delta\phi_i$ between the receiving and emitting compartment
262 (a number between -1 and 1) is recorded for the three i -identities ($i = cis, medial, trans$). Averaged
263 over all budding/fusion events, this defines the *enrichment vector* \vec{E} , whose three components
264 E_i are normalized for readability so that $\sum_i |E_i| = 1$ (see Fig.1A - App.6, p.37 for non-normalized
265 enrichment). Vesicular flux is predominantly anterograde if $E_{cis} < 0$ and $E_{trans} > 0$, while it is
266 predominantly retrograde if $E_{cis} > 0$ and $E_{trans} < 0$.

267 We focus on systems containing comparable amounts of each species at steady-state ($k_m = 1$
268 - see Eq.6). The enrichment in *cis*, *medial* and *trans*-identities are shown in Fig.3B as a function
269 of the budding rate k_b . The most striking result is the high correlation between purity of the
270 compartment and the directionality of vesicular transport. **For low values of the budding rate**
271 ($k_b \ll 1$), compartments are well mixed (purity $\lesssim 1/2$) and the vesicular flux is retrograde, with a
272 gain in *cis*-identities and a loss in *trans*-identities. **For high values of the budding rate** ($k_b \gg 1$),
273 compartments are pure (purity $\simeq 1$) and the vesicular flux is anterograde, with a gain in *trans*-
274 identities and a loss in *cis*-identities. The archetypal behaviors most often discussed in the literature
275 are thus, within the limits of our model, asymptotic regimes for extreme values of the ratio of
276 budding to fusion rates. Remarkably, the cross over between these two asymptotic behaviors
277 is rather broad ($k_b \sim 0.1 - 1$) and displays a more complex vesicular transport dynamics, mostly
278 oriented toward medial compartments.

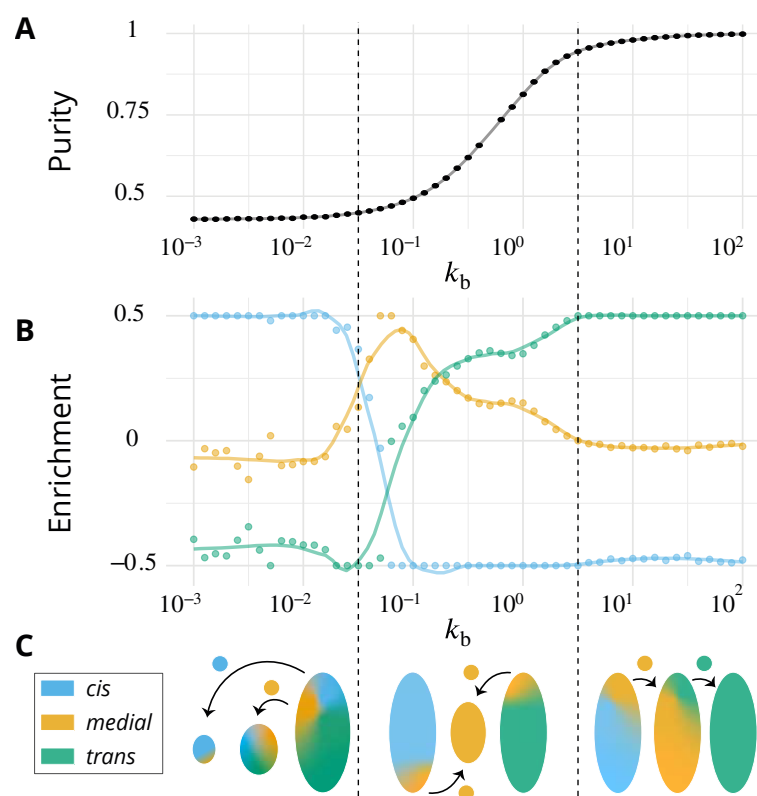


Figure 3. Directionality of vesicular transport, displayed varying the budding rate k_b for a biochemical conversion rate $k_m = 1$ (equal amount of all species in the system). (A) System purity as a function of the budding rate – a cut through the purity phase diagram shown Fig. 2 C. (B) Normalized enrichment in *cis* (blue), *medial* (orange) and *trans* (green) identities between the acceptor and donor compartments during vesicular exchange (solid lines are guides for the eyes). See App.6, p.37 for non-normalized fluxes. (C) Sketches showing the direction of the dominant vesicular fluxes – consistent with data of A and B and data from Fig.1 App.6 – omitting less contributive transports. Before the purity transition (low values of k_b - purity ~ 0.5) the vesicular flux is retrograde. After the transition (high values of k_b - purity ~ 1) the vesicular flux is anterograde. Around the crossover ($k_b \sim 0.1$), the vesicular flux is centripetal and oriented toward *medial*-compartments. The centripetal flux disappears if inter-compartments fusion is prohibited, see App.8, p.41.

In our model organelle, vesicle budding and fusion are biased solely by local compositions, which is subjected to irreversible biochemical conversions. The interplay between these microscopic processes gives rise to an irreversible flux of vesicles across the system. To better understand the directionality of vesicular exchanges, the net vesicular flux leaving compartments with a given composition is represented as a vector field in the compartments composition space in Fig.4. This is shown as a triangle plots in which each point corresponds to a fraction of *cis*, *medial* and *trans* components in a compartment, and the three vertices of the triangle correspond to pure compartments (see App.2). The variation of the vesicular flux with the budding rate k_b (Fig.4) is consistent with that of the composition enrichment in the different identities (Fig.3B). As k_b increases, the flux evolves from being mostly retrograde at low k_b (from *trans*-rich toward less mature compartments) to being anterograde at high k_b (from *cis* to *medial*, and *medial* to *trans* compartments). In between, the vesicular flux is centripetal toward mixed compartments, leading to a net enrichment in *medial*-identity. The relationship between structure and transport is explained below, and a dissection of this fluxes with respect to the composition of the vesicles is shown in App.6. The net flux leaving a particular region of the triangular phase space is proportional to the total system's size (number of compartments times their size) with this composition, while the flux arriving at a particular region depends on the number of compartments with that composition. Both quantities are shown on Fig.4.

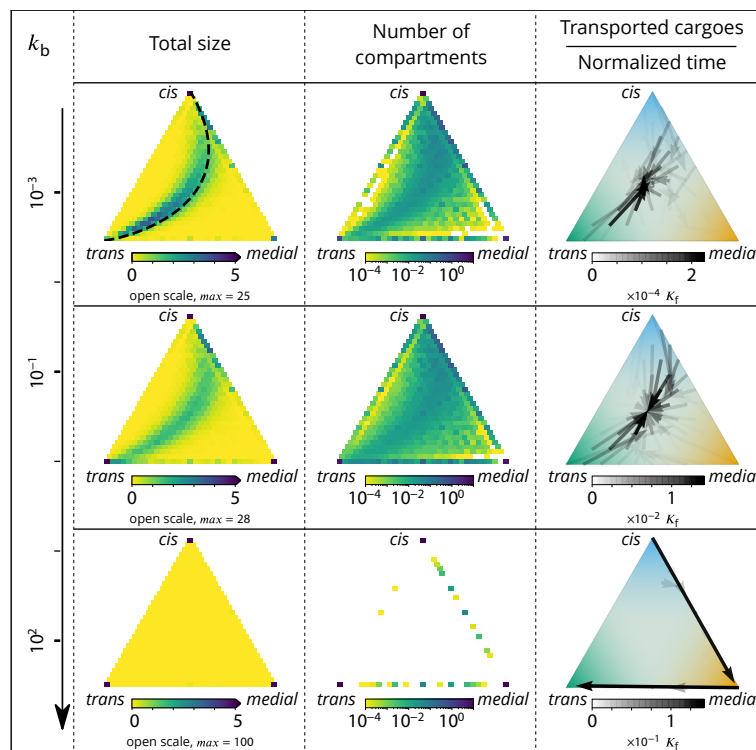


Figure 4. Relationship between the structure of the system and the vesicular fluxes. Distribution of the total size of the system (truncated scale, maximum value in brackets) and number of compartments, and the vesicular flux between them, shown in a triangular composition space. Each point represents a given composition of compartments and the triangle vertices are compartments of pure *cis*, *medial* and *trans* identity. Arrows show the vesicular flux. The base of each arrow is the composition of the donor compartment and the tip is the average composition of receiving compartments (ignoring back fusion). The opacity of the arrows is proportional to the flux of transported cargo going through this path per unit time ($1/K_f$), normalized by the total number of cargo-proteins. The dashed line on the top-left triangle is the theoretical prediction given by Eq.9. See also App.6 p.36 for further characterizations of the vesicular transport, and App.8 p.41 to discuss the impact of other budding and fusion implementations on the vesicular fluxes.

297 At low budding rate ($k_b \ll 1$ - top row in Fig.4), the system is in the mixed regime, where
 298 compartments are large (hundreds of vesicles in size) but mixed (purity $\lesssim 1/2$). The system is
 299 dominated by compartment maturation, and the compartment distribution is spread around a
 300 path going from purely *cis* to purely *trans*-compartments, consistent with a dynamics where each
 301 compartment matures independently from the other and given by Eq.9. - see top left panel
 302 of Fig.4. The majority of the transport vesicles are emitted by *trans*-rich compartments, which
 303 concentrate most of the components of the system, leading to a retrograde vesicular flux. Note
 304 that although vesicular flux is clearly retrograde in the maturation-dominated regime, as seen
 305 from the increase in *cis* identity and the decrease in *trans* identity between emitting and receiving
 306 compartment (Fig.3B), there is no net flux of vesicles from *medial*-rich to *cis* compartments in this
 307 limit (Fig.4). This differs from the classical “cisternal progression & maturation” mechanism sketched
 308 in Fig.1A, and is due to the fact that the compartments that contain the highest fraction of *medial*
 309 identity in this regime are well mixed ($\phi_{cis} \simeq \phi_{medial} \simeq \phi_{trans} \simeq 1/3$). The vesicular flux leaving such
 310 compartments is equally split into *cis*, *medial* and *trans* vesicles, which fuse homotypically with
 311 compartments enriched in their identity, yielding a vanishing net flux averaged over the three
 312 identities. There is nevertheless a strong retrograde flux of *cis* vesicles toward *cis* compartments,
 313 as shown in App.6 Fig.1. In the classical “cisternal maturation” mechanism, retrograde transport
 314 is needed to recycle *cis*-Golgi components from more mature compartments. Within the present
 315 model, this can be achieved by targeting such components to *cis* vesicles budding from more

316 mature compartments.

317 At high budding rate ($k_b \gg 1$ - bottom row in Fig.4), the system is in the vesicular regime,
318 where compartments are fairly pure, but rather small, with a size equivalent to a few vesicles.
319 Compartments are exclusively distributed along the *cis/medial* and *medial/trans*-axes of composition,
320 and accumulate at the vertices of the triangle. Membrane patches that just underwent conversion
321 bud quickly from the donor compartment and fuse with pure compartments with the appropriate
322 *medial* or *trans*-identity, explaining the clear anterograde vesicular transport. This feature is further
323 reinforced under very high budding rate, where the vesicular flux is dominated by budding vesicles
324 undergoing biochemical conversion *before* fusion, which prohibits their back fusion with the donor
325 compartment.

326 In the intermediate regime (middle row in Fig.4), the distribution of mixed compartments is
327 more homogeneous along the line describing the maturation of individual compartments - both in
328 terms of size and number of compartments. *Cis*-rich and *trans*-rich compartments emit comparable
329 amount of transport vesicles, while large *medial*-rich compartments are absent. This leads to a
330 centripetal vesicular flux with an enrichment in *medial* identity (see Fig.3 B). The lack of large *medial*-
331 rich compartment is due to the fact that they can be contaminated by either *cis* or *trans*-species
332 and fuse with *cis*-rich or *trans*-rich compartments. If inter-compartment fusion is prohibited, the
333 enrichment in medial-identity in the intermediate regime is abolished, with a direct transition from
334 anterograde to retrograde vesicular transport upon increasing k_b (see App.8 and the Discussion
335 section).

336 A graphical sketch consistent with our numerical observations for the typical size and composition
337 of different compartments and for the dominant vesicular fluxes between them in the different
338 regimes is shown in Fig.3C.

339 Discussion

340 The genesis and maintenance of complex membrane-bound organelles such as the Golgi apparatus
341 rely on self-organisation principles that are yet to be fully understood. Here we present a minimal
342 model in which steady-state Golgi-like structures spontaneously emerge from the interplay between
343 three basic mechanisms: the biochemical conversion of membrane components, the composition-
344 dependent vesicular budding, and inter-compartment fusion. As our model does not include space,
345 we do not refer to the spatial structure of a stacked Golgi, but rather to the self-organisation of Golgi
346 components into compartments of distinct identities undergoing vesicular exchange. We show
347 that directional vesicular exchanges between compartments of different identities spontaneously
348 emerge from local biochemical interactions, despite the absence of spatial information. This is in
349 line with recent observations that the Golgi functionality is preserved under major perturbation
350 of its spatial structure resulting from land-locking Golgi cisternae to mitochondria (Dunlop et al.,
351 2017). Indeed, cargo transport still proceed, and is merely slowed down by a factor of two (from 20
352 min. to 40 min.) in land-locked Golgi despite the absence of spatial proximity between cisternae.
353 This suggests that spatial information is less crucial to the Golgi function than biochemical infor-
354 mation. Our main result is that the steady-state organisation of the organelle, in terms of size and
355 composition of its compartments, is intimately linked to the directionality of vesicular exchange
356 between compartments through the mechanism of homotypic fusion. Both aspects are controlled
357 by a kinetic competition between vesicular exchange and biochemical conversion.

358 The results presented in Fig.2 can be used to explain a number of experimental observations.
359 The predicted role of the **budding and fusion rates** is in agreement with the phenotype observed
360 upon deletion of Arf1 (a protein involved in vesicle budding), which decreases the number of
361 compartments and increases their size, particularly that of *trans*-compartments which seem to
362 aggregate into one major cisterna (Bhave et al., 2014). A comparable phenotype has been observed
363 upon mutation of NSF (a fusion protein), which produces extremely large, but transient, *trans*-
364 compartments (Tanabashi et al., 2018), thereby increasing the stochasticity of the system. This
365 is consistent with an increase of the fusion rate according to our model (see App.5, p.34 for a

366 quantification of the fluctuations in our model). Modifying the expression of *VPS74* (yeast homolog
367 of *GOLPH3*) leads to an altered Golgi organisation, comparable to the *ARF1* deletion phenotype
368 (*Iyer et al., 2018*). Both $\Delta arf1$ and $\Delta vps74$ present an enlargement of the Golgi cisternae and a
369 disruption of molecular gradients in the system, which we interpret, in the limits of our system,
370 as a lower purity due to slower sorting kinetics following an impairment of the budding dynamics.
371 Importantly, the correlation between the size and purity of the compartments predicted by our
372 model is in agreement with the observation that decreasing the budding rate by altering the activity
373 of COPI (a budding protein) leads to larger and less sorted compartments (*Papanikou et al., 2015*).
374 In yeast again, over-expression of Ypt1 (a Rab protein) increases the transition rate from early to
375 transitional Golgi, and increases the co-localization of early and late Golgi markers (*Kim et al., 2016*).
376 We interpret this as a decrease of the purity of Golgi cisternae upon increasing the biochemical
377 conversion rate by unbalancing the ratio of budding to conversion rates. This suggests that the
378 wild-type Yeast Golgi is closed to the line $k_m = k_b$ shown in Fig.2.

379 One crucial model prediction is that the size and purity of Golgi compartments should be affected
380 in a correlated fashion by physiological perturbations. This could be tested experimentally by further
381 exploring the phase diagrams of Fig.2B-C by simultaneously varying the ratios of biochemical
382 conversion over fusion rate k_m and of budding over fusion rate k_b . Compartment purity can be
383 altered without changing their size by acting on k_m , while it should be correlated with a change of
384 size by acting on k_b . We thus predict that the purity decrease concomitant with the size increase
385 observed in *Papanikou et al. (2015)* upon **impairing COP-I activity** (decreasing k_b) could be reversed
386 *without a change of cisterna size* upon decreasing the biochemical conversion rate k_m , e.g. by
387 impairing Ypt1 activity (as done in *Kim et al. (2016)*). Along the same line, we predict that the
388 decrease of purity observed by *Kim et al. (2016)* upon Ypt1 over-expression (which increases the
389 early to transitional conversion rate) should not be associated to change of cisternae size (at steady-
390 state) if altering Ypt1 does not modify the budding rate k_b . We can predict further that the loss of
391 purity phenotype could be reversed upon increasing the budding rate by over-expressing COP-I,
392 but that this would be accompanied by an decrease of cisternae size. This experimental proposal
393 is represented graphically on the size and purity phase diagrams in App.9 Fig.1, with somewhat
394 contrary arrows, to give a feel for the way our model may be used to design experimental strategies.

395 The directionality of vesicular transport is intimately linked to the steady-state organisation of
396 the organelle; vesicular transport is anterograde when compartments are pure, and it is retrograde
397 when they are mixed. This can be intuitively understood with the notion of “contaminating species”.
398 If a compartment enriched in a particular molecular identity emits a vesicle of that identity, the
399 vesicle will likely fuse back with the emitting compartment by homotypic fusion, yielding no vesicular
400 exchange. On the other hand, an emitted vesicle that contains a minority (contaminating) identity
401 will homotypically fuse with another compartment. If budding is faster than biochemical conversion,
402 the contaminating species is the one that just underwent conversion, and its budding and fusion
403 with more mature compartment leads to an anterograde transport. In such systems, compartments
404 are rather small and pure. If biochemical conversion is faster than budding, the contaminating
405 species is the less mature one, leading to a retrograde transport. Such systems are rather mixed
406 with large compartments. Thus, the directionality of vesicular exchange is an emergent property
407 intimately linked to the purity of the compartments. The *medial*-rich compartments are special in
408 that regard: for intermediate values of the purity ($k_b \sim k_m$), they may be contaminated both by yet
409 to be matured *cis*-species and already matured *trans*-species and can fuse both with *cis*-rich and
410 *trans*-rich compartments. If inter-compartment fusion is allowed, large *medial*-rich compartments
411 are relatively scarce, and emit few vesicles. On the other hand, *medial*-vesicles emitted by *cis/medial*
412 and *medial/trans*-compartments may fuse together to form (small) *medial*-rich compartments.
413 For intermediate values of the budding rates, this vesicular flux dominates vesicular exchange
414 and leads to a centripetal vesicular flux towards *medial*-compartments (details in App.6, p.37).
415 If inter-compartment fusion is prohibited, which for instance corresponds to a situation where
416 Golgi cisternae are immobilized (*Dunlop et al., 2017*), *medial*-rich compartments are present at

417 steady-state, the centripetal vesicular flux is less intense, and the purity transition is accompanied
418 with a direct transition from retrograde to anterograde vesicular flux (App.8, p.41). Note that
419 vesicular transport of cargo through the Golgi is not bound to follow the net vesicular flux between
420 compartments discussed above. Indeed, the net flux is the average of the flux of vesicles of the
421 three identities. A given cargo follows this flux - on average - if it does not interact preferentially
422 with membrane of particular identity. On the other hand, a cargo that is preferentially packaged
423 into vesicles of *trans* identity (for example) will be transported toward *trans*-rich compartment even
424 if the net vesicular flux is mostly retrograde.

425 Regardless of the details of the model, we find that systems showing a well defined polarity with
426 well sorted cisternae exhibit anterograde vesicular fluxes, whereas systems with mixed compart-
427 ments exhibit retrograde fluxes. The former dynamics is expected when biochemical conversion
428 is the slowest kinetic process and compartments are long-lived, while the latter is expected when
429 vesicular exchange is slow and the system is composed of transient compartments undergoing
430 individual maturation. One can relate this prediction to the difference in organisation and dynamics
431 between the Golgi of *S. cerevisiae* and the more organized Golgi of higher organisms such as
432 vertebrates. Maturation of Golgi cisternae has been directly observed in *S. cerevisiae* (*Losev et al., 2006*),
433 with colocalization of different identity markers within single cisternae (low purity) during
434 maturation, whereas vesicular transport phenotypes have been indirectly observed (*Dunlop et al., 2017*) or inferred through modeling (*Dmitrieff et al., 2013*) in mammalian cells. Consistent with
435 our predictions, Golgi dynamics is one to two orders of magnitude faster in *S. cerevisiae* Golgi
436 cisternae (as measured by the typical maturation rate of cisternae $\sim 1/\text{min}$. (*Losev et al., 2006*;
437 *Matsuura-Tokita et al., 2006*)) than in mammalian cells (as measured by the typical Golgi exit rate
438 of cargo $\sim 1/20 \text{ min.}$ to $\sim 1/40 \text{ min.}$ (*Bonfanti et al., 1998; Hirschberg et al., 1998; Patterson et al., 2008; Boncompain et al., 2012*)). At this point, one may speculate a link between structure and
439 function through kinetics. A well sorted and polarized Golgi is presumably required to accurately
440 process complex cargo. The glycosylation of secreted cargo is key to the interaction of a vertebrate
441 cell with the immune system of the organism it belongs to (*Ryan and Cobb, 2012*), and glycans
442 appear to be more diverse in higher eukaryotes - which also possess a highly organized Golgi - than
443 in unicellular eukaryotes like yeast (*Wang et al., 2017*). The Golgi organisation in *S. cerevisiae* could
444 thus be the result of an adaptation that has favored fast transport over robustness of processing,
445 leading to a less organized Golgi characterized by cisternal maturation and retrograde vesicular
446 transport. Remarkably, the slowing down of Golgi transport when *S. cerevisiae* is starved in a
447 glucose-free environment coincides with the Golgi becoming more polarized (*Levi et al., 2010*),
448 strengthening the proposal derived from our model of a strong connection between transport
449 kinetics and steady-state Golgi structure.

450 The present model is designed to account for crucial dynamical processes at play in the Golgi
451 with a limited number of parameters. It is sufficient to yield robust self-organised structures which
452 can reproduce a number of experimental observations, but cannot be expected to account for
453 the full richness of Golgi dynamics, especially under severe perturbation. The model includes
454 a single kind of exchange mechanism based on vesicles. Exchange could also proceed via the
455 pinching and fusion of larger cisterna fragments (*Pfeffer, 2010; Dmitrieff et al., 2013*), or via tubular
456 connection between compartments (*Trucco et al., 2004*), although the relevance of the latter to
457 Golgi transport is still debated (*Glick and Luini, 2011*). Exchange mechanisms that do not establish
458 stable connections able to relax concentration gradient between compartments by diffusion could
459 be included as extension of our vesicle exchange mechanism (at the expense of introducing
460 additional parameters to characterise their composition and size-dependent nucleation, scission
461 and fusion rates). Stable Golgi tubulation without tubule detachment is observed under brefeldin
462 A treatment, which prevent the membrane association of COPI coat. This eventually leads to
463 the disappearance of the Golgi by quick resorption into the ER whenever a tubular connection
464 is established between them, in a way suggesting a purely physical (tension-driven) mechanism
465 (*Sciaky et al., 1997*). According to our model, preventing COPI vesicle budding should lead to larger

468 cisternae, as discussed above. The brefeldin A phenotype can be reconciled with our framework
469 by invoking the fact that larger cisternae should have a higher surface to volume ratio and hence
470 a lower membrane tension, decreasing the force required to nucleate membrane tubules and
471 increasing the probability of direct tubular connection with the ER. Such tension effects are clearly
472 beyond the scope of the present model, but this phenotype could be qualitatively reproduced
473 by invoking an increase of the ER fusion parameter α_{ER} with the size of the compartment due to
474 membrane mechanics considerations.

475 The model does not account for the possibility of lateral partitioning between processing and
476 exporting domains within compartments which could play an important role in regulating cisterna
477 composition and cargo process^{SSD}g (**Patterson et al., 2008**). A detailed kinetic model of organisation
478 based on this concept and supported by extensive quantitative live cell imaging experiments is
479 proposed in (**Patterson et al., 2008**) to account for the distinct composition of the different Golgi
480 cisterna and the kinetics of cargo transport. This rapid partitioning model (RPM) is very different
481 in scope with the model we propose here, since it focuses on the transport of lipids and cargo
482 molecules in a pre-established Golgi apparatus with a prescribed structure, while the present model
483 describes de-novo Golgi formation and maintenance, through self-organised fusion and scission
484 mechanisms between dynamic compartments. The two models share important similarities, such
485 as the fact that no directionality is assumed a priori for intra-cisternal vesicular transport, and
486 that export is allowed from every cisterna, which is crucial to reproduce the exponential kinetics
487 observed in experiments. The RPM is much more precise in terms of the microscopic description of
488 the biochemical processes, and consequently involves many parameters. Combining our simple
489 model of Golgi self-organisation with the detailed description given by the RPM for the kinetics of
490 lipid, enzymes and cargo within the Golgi is the logical next step to push forward our understanding
491 of Golgi self-organisation.

492 In summary, we have analyzed a model of self-organisation and transport in cellular organelles
493 based on a limited number of kinetic steps allowing for the generation and biochemical conversion
494 of compartments, and vesicular exchange between them. Although we kept the complexity of
495 individual steps to a minimum, our model gives rise to a rich diversity of phenotypes depending
496 on the parameter values, and reproduces the effect of a number of specific protein mutations.
497 We identify the concomitance of a structural transition (from large and mixed to small and pure
498 sub-compartments) and a dynamical transition (from retrograde to anterograde vesicular exchange).
499 Within our model, anterograde vesicular transport is accompanied by many spurious events of
500 vesicle back-fusion. For very high budding rates, compartments are very pure and anterograde
501 transport is dominated by vesicles undergoing biochemical conversion *after* budding from a com-
502 partment. In our model, such vesicle biochemical conversion events, which have been described
503 in the secretory pathway as a way to direct vesicular traffic and to prevent vesicles back-fusion
504 (**Lord et al., 2011**), only occur when compartments are very small (high budding rate). **Adding**
505 **composition-dependent feedback involving specific molecular actors to tune budding and fusion**
506 **rates - for instance to reduce or prevent the budding of the majority species - will displace the**
507 **purity transition to lower budding rates and thus extend the regime of anterograde transport to**
508 **larger sub-compartment steady-state sizes. Cisternal stabilizers like GRASP or vesicles careers like**
509 **Golgins, known to already be present in the ancestor of eukaryotes** (**Barlow et al., 2018**), are obvious
510 candidates. Although more complex models, and in particular the inclusion of spatial dependencies,
511 are surely relevant to dynamics of the organelle, the fundamental relationship between kinetics,
512 structure and transport highlighted by our model is a universal feature of the interplay between
513 biochemical conversion and vesicular exchange in cellular organelles.

514 Acknowledgments

515 We acknowledge stimulating discussions with Bruno Goud, Cathy Jackson, Grégory Lavieu, Franck
516 Perez and Stéphanie Miserey-Lenkei, and critical reading of the manuscript by Matthew S. Turner.

517 **Competing interests**

518 The authors declare no conflict of interest.

519 **Nomenclature**

520 Here is the nomenclature used in the main text and Appendix sections.

Table 1. System's parameters

K_b	Budding rate per patches of membrane in a compartment
K_m	biochemical conversion rate for each patch of membrane (<i>cis</i> → <i>medial</i> → <i>trans</i>)
K_f	Maximum fusion rate between two compartments
J	Injection rate of <i>cis</i> -vesicles from the ER
k_b	Budding rate normalized by the fusion rate (K_b/K_f)
k_m	biochemical conversion rate normalized by the fusion rate (K_m/K_f)
j	Injection rate normalized by the fusion rate (J/K_f)
α	Fraction of active species (driving homotypic fusion) in the ER (<i>cis</i>) or the TGN (<i>trans</i>)
α_i	When different between boundaries, α in the boundary i (i equals ER or TGN)

Table 2. Compartments' description

ϕ_i	Fraction of a given species i (<i>cis</i> , <i>medial</i> or <i>trans</i>) in a compartment
\vec{C}	Composition of a compartment, whose components are the fractions ϕ_i
n	Size of a compartment, (<i>i.e.</i> number of membrane patches in the compartment)
n_i	Number of membrane patches of the i identity, in a compartment
n_{id}	Number of different identities (from 1 to 3) in a single a compartment
n_v	Number of vesicles surrounding a compartment that share its composition
P	Purity of a compartment
$J_{b,i}$	Budding flux of vesicles decorated by the identity i , from a compartment

Table 3. Steady-state description

c_n	Size distribution of compartments in the system
n_c	Cutoff in the size distribution, namely the typical size of big compartments
N	Total number of membrane patches, in all compartments, in the steady-state system
N_i	Total number of patches of the i species (<i>cis</i> , <i>medial</i> or <i>trans</i>)

521 **References**

- 522 Antonin W, Holroyd C, Tikkanen R, Höning S, Jahn R. The R-SNARE endobrevin/VAMP-8 mediates homotypic
523 fusion of early endosomes and late endosomes. *Molecular Biology of the Cell*. 2000 Oct; 11(10):3289–3298.
- 524 Barlow LD, Nývltová E, Aguilar M, Tachezy J, Dacks JB. A sophisticated, differentiated Golgi in the ancestor of
525 eukaryotes. *BMC Biology*. 2018 Mar; 16:27. <https://doi.org/10.1186/s12915-018-0492-9>.
- 527 Bekier MEn, Wang L, Li J, Huang H, Tang D, Zhang X, Wang Y. Knockout of the Golgi stacking proteins GRASP55
528 and GRASP65 impairs Golgi structure and function. *Molecular biology of the cell*. 2017 10; 28(21):2833–2842.
529 <https://www.ncbi.nlm.nih.gov/pubmed/28814501>, doi: 10.1091/mbc.E17-02-0112.
- 530 Bhave M, Papanikou E, Iyer P, Pandya K, Jain BK, Ganguly A, Sharma C, Pawar K, Austin J, Day KJ, Rossanese
531 OW, Glick BS, Bhattacharyya D. Golgi enlargement in Arf-depleted yeast cells is due to altered dynamics of
532 cisternal maturation. *Journal of Cell Science*. 2014 Jan; 127(Pt 1):250–257. doi: 10.1242/jcs.140996.

- 533 **Binder B**, Goede A, Berndt N, Holzhütter HG. A conceptual mathematical model of the dynamic self-organisation
534 of distinct cellular organelles. *PloS One*. 2009 Dec; 4(12):e8295. doi: [10.1371/journal.pone.0008295](https://doi.org/10.1371/journal.pone.0008295).
- 535 **Boncompain G**, Divoux S, Gareil N, de Forges H, Lescure A, Latreche L, Mercanti V, Jollivet F, Raposo G, Perez F.
536 Synchronization of secretory protein traffic in populations of cells. *Nature Methods*. 2012 Mar; 9(5):493–498.
537 doi: [10.1038/nmeth.1928](https://doi.org/10.1038/nmeth.1928).
- 538 **Boncompain G**, Perez F. The many routes of Golgi-dependent trafficking. *Histochemistry and Cell Biology*. 2013
539 Sep; 140(3):251–260. doi: [10.1007/s00418-013-1124-7](https://doi.org/10.1007/s00418-013-1124-7).
- 540 **Bonfanti L**, Mironov AA, Martínez-Menárguez JA, Martella O, Fusella A, Baldassarre M, Buccione R, Geuze HJ,
541 Mironov AA, Luini A. Procollagen traverses the Golgi stack without leaving the lumen of cisternae: evidence
542 for cisternal maturation. *Cell*. 1998 Dec; 95(7):993–1003.
- 543 **Bonifacino JS**, Glick BS. The mechanisms of vesicle budding and fusion. *Cell*. 2004 Jan; 116(2):153–166.
- 544 **Cai H**, Reinisch K, Ferro-Novick S. Coats, tethers, Rabs, and SNAREs work together to mediate the
545 intracellular destination of a transport vesicle. *Developmental Cell*. 2007 May; 12(5):671–682. doi:
546 [10.1016/j.devcel.2007.04.005](https://doi.org/10.1016/j.devcel.2007.04.005).
- 547 **Day KJ**, Staehelin LA, Glick BS. A Three-Stage Model of Golgi Structure and Function. *Histochemistry and cell biology*.
548 2013 Sep; 140(3):239–249. <http://www.ncbi.nlm.nih.gov/pmc/articles/PMC3779436/>, doi: [10.1007/s00418-013-1128-3](https://doi.org/10.1007/s00418-013-1128-3).
- 549 **Dmitrieff S**, Sens P. Cooperative protein transport in cellular organelles. *Physical Review E, Statistical, Nonlinear,
550 and Soft Matter Physics*. 2011 Apr; 83(4 Pt 1):041923. doi: [10.1103/PhysRevE.83.041923](https://doi.org/10.1103/PhysRevE.83.041923).
- 551 **Dmitrieff S**, Rao M, Sens P. Quantitative analysis of intra-Golgi transport shows intercisternal exchange for
552 all cargo. *Proceedings of the National Academy of Sciences of the United States of America*. 2013 Sep;
553 110(39):15692–15697. doi: [10.1073/pnas.1303358110](https://doi.org/10.1073/pnas.1303358110).
- 554 **Dunlop MH**, Ernst AM, Schroeder LK, Toomre DK, Lavieu G, Rothman JE. Land-locked mammalian Golgi reveals
555 cargo transport between stable cisternae. *Nature Communications*. 2017; 8(1):432. doi: [10.1038/s41467-017-00570-z](https://doi.org/10.1038/s41467-017-00570-z).
- 556 **Gillespie DT**. Exact stochastic simulation of coupled chemical reactions. *The Journal of Physical Chemistry*. 1977
557 Dec; 81(25):2340–2361. <https://doi.org/10.1021/j100540a008>, doi: [10.1021/j100540a008](https://doi.org/10.1021/j100540a008).
- 558 **Glick BS**, Luini A. Models for Golgi Traffic: A Critical Assessment. *Cold Spring Harbor Perspectives in Biology*.
559 2011 Nov; 3(11). <http://www.ncbi.nlm.nih.gov/pmc/articles/PMC3220355/>, doi: [10.1101/cshperspect.a005215](https://doi.org/10.1101/cshperspect.a005215).
- 560 **Gong H**, Guo Y, Linstedt A, Schwartz R. Discrete, continuous, and stochastic models of protein sorting in the
561 Golgi apparatus. *Physical Review E, Statistical, Nonlinear, and Soft Matter Physics*. 2010 Jan; 81(1 Pt 1):011914.
562 doi: [10.1103/PhysRevE.81.011914](https://doi.org/10.1103/PhysRevE.81.011914).
- 563 **Grosshans BL**, Ortiz D, Novick P. Rabs and their effectors: Achieving specificity in membrane traffic. *Proceedings
564 of the National Academy of Sciences*. 2006 Aug; 103(32):11821–11827. <http://www.pnas.org/content/103/32/11821>, doi: [10.1073/pnas.0601617103](https://doi.org/10.1073/pnas.0601617103).
- 565 **Heald R**, Cohen-Fix O. Morphology and function of membrane-bound organelles. *Current Opinion in Cell
566 Biology*. 2014 Feb; 26:79–86. doi: [10.1016/j.ceb.2013.10.006](https://doi.org/10.1016/j.ceb.2013.10.006).
- 567 **Hirschberg K**, Miller CM, Ellenberg J, Presley JF, Siggia ED, Phair RD, Lippincott-Schwartz J. Kinetic Analysis of
568 Secretory Protein Traffic and Characterization of Golgi to Plasma Membrane Transport Intermediates in Living
569 Cells. *The Journal of Cell Biology*. 1998 Dec; 143(6):1485–1503. <http://jcb.rupress.org/content/143/6/1485>, doi:
570 [10.1083/jcb.143.6.1485](https://doi.org/10.1083/jcb.143.6.1485).
- 571 **Hu W**, Xu R, Zhang G, Jin J, Szulc ZM, Bielawski J, Hannun YA, Obeid LM, Mao C. Golgi Fragmentation Is Associated
572 with Ceramide-induced Cellular Effects. *Mol Biol Cell*. 2005; 16:1555–1567.
- 573 **Ispolatov I**, Müsch A. A model for the self-organization of vesicular flux and protein distributions in the Golgi
574 apparatus. *PLoS computational biology*. 2013; 9(7):e1003125. doi: [10.1371/journal.pcbi.1003125](https://doi.org/10.1371/journal.pcbi.1003125).
- 575 **Iyer P**, Bhave M, Jain BK, RoyChowdhury S, Bhattacharyya D. Vps74p controls Golgi size in an Arf1-dependent
576 manner. *FEBS letters*. 2018 Oct; doi: [10.1002/1873-3468.13266](https://doi.org/10.1002/1873-3468.13266).
- 577 **Kelly RB**. Pathways of protein secretion in eukaryotes. *Science (New York, NY)*. 1985 Oct; 230(4721):25–32.
- 578

- 581 **Kim JJ**, Lipatova Z, Majumdar U, Segev N. Regulation of Golgi Cisternal Progression by Ypt/Rab GTPases.
582 *Developmental Cell*. 2016 Feb; 36(4):440–452. doi: [10.1016/j.devcel.2016.01.016](https://doi.org/10.1016/j.devcel.2016.01.016).
- 583 **Klemm RW**, Ejsing CS, Surma MA, Kaiser HJ, Gerl MJ, Sampaio JL, de Robillard Q, Ferguson C, Proszynski TJ,
584 Shevchenko A, Simons K. Segregation of sphingolipids and sterols during formation of secretory vesicles at
585 the trans-Golgi network. *The Journal of Cell Biology*. 2009 May; 185(4):601–612. doi: [10.1083/jcb.200901145](https://doi.org/10.1083/jcb.200901145).
- 586 **Klute MJ**, Melançon P, Dacks JB. Evolution and diversity of the Golgi. *Cold Spring Harbor Perspectives in Biology*.
587 2011 Aug; 3(8):a007849. doi: [10.1101/cshperspect.a007849](https://doi.org/10.1101/cshperspect.a007849).
- 588 **Kühnle J**, Shillcock J, Mouritsen OG, Weiss M. A modeling approach to the self-assembly of the Golgi apparatus.
589 *Biophysical Journal*. 2010 Jun; 98(12):2839–2847. doi: [10.1016/j.bpj.2010.03.035](https://doi.org/10.1016/j.bpj.2010.03.035).
- 590 **Lavieu G**, Zheng H, Rothman JE. Stapled Golgi cisternae remain in place as cargo passes through the stack.
591 *eLIFE*. 2013; 2:e00558.
- 592 **Levi SK**, Bhattacharyya D, Strack RL, Austin JR, Glick BS. The Yeast GRASP Grh1 Colocalizes with COPII and Is
593 Dispensable for Organizing the Secretory Pathway. *Traffic* (Copenhagen, Denmark). 2010 Sep; 11(9):1168–
594 1179. <https://www.ncbi.nlm.nih.gov/pmc/articles/PMC2919637/>, doi: [10.1111/j.1600-0854.2010.01089.x](https://doi.org/10.1111/j.1600-0854.2010.01089.x).
- 595 **Lippincott-Schwartz J**, Roberts TH, Hirschberg K. Secretory protein trafficking and organelle dynamics
596 in living cells. *Annual Review of Cell and Developmental Biology*. 2000; 16:557–589. doi: [10.1146/annurev.cellbio.16.1.557](https://doi.org/10.1146/annurev.cellbio.16.1.557).
- 598 **Lord C**, Bhandari D, Menon S, Ghassemian M, Nycz D, Hay J, Ghosh P, Ferro-Novick S. Sequential interactions
599 with Sec23 control the direction of vesicle traffic. *Nature*. 2011 May; 473(7346):181–186. <https://www.ncbi.nlm.nih.gov/pmc/articles/PMC3093450/>, doi: [10.1038/nature09969](https://doi.org/10.1038/nature09969).
- 601 **Losev E**, Reinke CA, Jellen J, Strongin DE, Bevis BJ, Glick BS. Golgi maturation visualized in living yeast. *Nature*.
602 2006 Jun; 441(7096):1002–1006. <https://www.nature.com/nature/journal/v441/n7096/full/nature04717.html>,
603 doi: [10.1038/nature04717](https://doi.org/10.1038/nature04717).
- 604 **Malhotra V**, Mayor S. Cell biology: The Golgi grows up. *Nature*. 2006 Jun; 441(7096):939–940. <https://www.nature.com/articles/441939a>, doi: [10.1038/441939a](https://doi.org/10.1038/441939a).
- 606 **Marra P**, Salvatore L, Mironov A, Di Campli A, Di Tullio G, Trucco A, Beznoussenko G, Mironov A, De Matteis
607 MA. The biogenesis of the Golgi ribbon: the roles of membrane input from the ER and of GM130. *Molecular
608 Biology of the Cell*. 2007 May; 18(5):1595–1608. doi: [10.1091/mbc.E06-10-0886](https://doi.org/10.1091/mbc.E06-10-0886).
- 609 **Marsh BJ**, Volkmann N, McIntosh JR, Howell KE. Direct continuities between cisternae at different levels of the
610 Golgi complex in glucose-stimulated mouse islet beta cells. *Proceedings of the National Academy of Sciences
611 of the United States of America*. 2004 Apr; 101(15):5565–5570. doi: [10.1073/pnas.0401242101](https://doi.org/10.1073/pnas.0401242101).
- 612 **Matsuura-Tokita K**, Takeuchi M, Ichihara A, Mikuriya K, Nakano A. Live imaging of yeast Golgi cisternal
613 maturation. *Nature*. 2006 Jun; 441(7096):1007–1010. doi: [10.1038/nature04737](https://doi.org/10.1038/nature04737).
- 614 **McDermott MI**, Mousley CJ. Lipid transfer proteins and the tuning of compartmental identity in the Golgi
615 apparatus. *Chemistry and Physics of Lipids*. 2016; 200:42–61.
- 616 **Mukherji S**, O’Shea EK. Mechanisms of organelle biogenesis govern stochastic fluctuations in organelle
617 abundance. *eLife*. 2014 Jun; 3:e02678.
- 618 **Papanikou E**, Day KJ, Austin J, Glick BS. COPI selectively drives maturation of the early Golgi. *eLife*. 2015 Dec; 4.
619 doi: [10.7554/eLife.13232](https://doi.org/10.7554/eLife.13232).
- 620 **Patterson GH**, Hirschberg K, Polishchuk RS, Gerlich D, Phair RD, Lippincott-Schwartz J. Transport through the
621 Golgi Apparatus by Rapid Partitioning within a Two-Phase Membrane System. *Cell*. 2008 Jun; 133(6):1055–1067.
622 <http://www.sciencedirect.com/science/article/pii/S0092867408006181>, doi: [10.1016/j.cell.2008.04.044](https://doi.org/10.1016/j.cell.2008.04.044).
- 623 **Pfeffer SR**. How the Golgi works: a cisternal progenitor model. *Proceedings of the National Academy of Sciences
624 of the United States of America*. 2010 Nov; 107(46):19614–19618. doi: [10.1073/pnas.1011016107](https://doi.org/10.1073/pnas.1011016107).
- 625 **Presley JF**, Cole NB, Schroer TA, Hirschberg K, Zaal KJ, Lippincott-Schwartz J. ER-to-Golgi transport visualized in
626 living cells. *Nature*. 1997 Sep; 389(6646):81–85. doi: [10.1038/38001](https://doi.org/10.1038/38001).
- 627 **Rink J**, Ghigo E, Kalaidzidis Y, Zerial M. Rab conversion as a mechanism of progression from early to late
628 endosomes. *Cell*. 2005 Sep; 122(5):735–749. doi: [10.1016/j.cell.2005.06.043](https://doi.org/10.1016/j.cell.2005.06.043).

- 629 **Rizzo R**, Parashuraman S, Mirabelli P, Puri C, Lucocq J, Luini A. The dynamics of engineered resident proteins in
630 the mammalian Golgi complex relies on cisternal maturation. *J Cell Biol*. 2013; 201:1027–1036.
- 631 **Ryan SO**, Cobb BA. Roles for major histocompatibility complex glycosylation in immune function. *Seminars in*
632 *Immunopathology*. 2012 May; 34(3):425–441. doi: 10.1007/s00281-012-0309-9.
- 633 **Sachdeva H**, Barma M, Rao M. Nonequilibrium description of de novo biogenesis and transport through
634 Golgi-like cisternae. *Scientific Reports*. 2016 Dec; 6:38840. doi: 10.1038/srep38840.
- 635 **Sciaky N**, Presley J, Smith C, Zaal KJ, Cole N, Moreira JE, Terasaki M, Siggia E, Lippincott-Schwartz J. Golgi
636 tubule traffic and the effects of brefeldin A visualized in living cells. *The Journal of Cell Biology*. 1997 Dec;
637 139(5):1137–1155.
- 638 **Sens P**, Rao M. (Re)modeling the Golgi. *Methods in Cell Biology*. 2013; 118:299–310. doi: [10.1016/B978-0-12-417164-0.00018-5](https://doi.org/10.1016/B978-0-12-417164-0.00018-5).
- 640 **Shen X**, Hong MS, Moss J, Vaughan M. BIG1, a brefeldin A-inhibited guanine nucleotide-exchange protein, is
641 required for correct glycosylation and function of integrin β 1A-inhibited guanine nucleotide-exchange protein,
642 is required for correct glycosylation and function of integrin β 1. *P Natl Acad Sci USA*. 2007; 104:1230–1235.
- 643 **Stanley P**. Golgi glycosylation. *Cold Spring Harbor Perspectives in Biology*. 2011 Apr; 3(4). doi: [10.1101/cshperspect.a005199](https://doi.org/10.1101/cshperspect.a005199).
- 645 **Suda Y**, Kurokawa K, Hirata R, Nakano A. Rab GAP cascade regulates dynamics of Ypt6 in the Golgi traffic.
646 *Proceedings of the National Academy of Sciences of the United States of America*. 2013 Nov; 110(47):18976–
647 18981. doi: [10.1073/pnas.1308627110](https://doi.org/10.1073/pnas.1308627110).
- 648 **Suda Yasuyuki**, Nakano Akihiko. The Yeast Golgi Apparatus. *Traffic*. 2011 Dec; 13(4):505–510. <https://onlinelibrary.wiley.com/doi/abs/10.1111/j.1600-0854.2011.01316.x>, doi: [10.1111/j.1600-0854.2011.01316.x](https://doi.org/10.1111/j.1600-0854.2011.01316.x).
- 650 **Tachikawa M**, Mochizuki A. Golgi apparatus self-organizes into the characteristic shape via postmitotic re-
651 assembly dynamics. *Proceedings of the National Academy of Sciences of the United States of America*. 2017
652 May; 114(20):5177–5182. doi: [10.1073/pnas.1619264114](https://doi.org/10.1073/pnas.1619264114).
- 653 **Takamori S**, Holt M, Stenius K, Lemke EA, Grønborg M, Riedel D, Urlaub H, Schenck S, Brügger B, Ringler P, Müller
654 SA, Rammner B, Gräter F, Hub JS, De Groot BL, Mieskes G, Moriyama Y, Klingauf J, Grubmüller H, Heuser J, et al.
655 Molecular anatomy of a trafficking organelle. *Cell*. 2006 Nov; 127(4):831–846. doi: [10.1016/j.cell.2006.10.030](https://doi.org/10.1016/j.cell.2006.10.030).
- 656 **Tanabashi S**, Shoda K, Saito C, Sakamoto T, Kurata T, Uemura T, Nakano A. A missense mutation in the NSF
657 gene causes abnormal Golgi morphology in *Arabidopsis thaliana*. *Cell Structure and Function*. 2018 Feb; doi:
658 [10.1247/csf.17026](https://doi.org/10.1247/csf.17026).
- 659 **Trucco A**, Polishchuk RS, Martella O, Pentima AD, Fusella A, Giandomenico DD, Pietro ES, Beznoussenko GV,
660 Polishchuk EV, Baldassarre M, Buccione R, Geerts WJC, Koster AJ, Burger KNJ, Mironov AA, Luini A. Secretory
661 traffic triggers the formation of tubular continuities across Golgi sub-compartments. *Nat Cell Biol*. 2004;
662 6(11):1071–1081.
- 663 **Turner MS**, Sens P, Socci ND. Nonequilibrium Raftlike Membrane Domains under Continuous Recycling.
664 *Physical Review Letters*. 2005 Oct; 95(16):168301. <https://link.aps.org/doi/10.1103/PhysRevLett.95.168301>, doi: [10.1103/PhysRevLett.95.168301](https://doi.org/10.1103/PhysRevLett.95.168301).
- 666 **Vagne Q**, Sens P. Stochastic Model of Maturation and Vesicular Exchange in Cellular Organelles. *Biophys J*. 2018;
667 114:947–957.
- 668 **Vagne Q**, Sens P. Stochastic Model of Vesicular Sorting in Cellular Organelles. *Physical Review Letters*.
669 2018 Feb; 120(5):058102. <https://link.aps.org/doi/10.1103/PhysRevLett.120.058102>, doi: [10.1103/PhysRevLett.120.058102](https://doi.org/10.1103/PhysRevLett.120.058102).
- 671 **Vagne Q**, Turner MS, Sens P. Sensing Size through Clustering in Non-Equilibrium Membranes and the Con-
672 trol of Membrane-Bound Enzymatic Reactions. *PloS One*. 2015; 10(12):e0143470. doi: [10.1371/journal.pone.0143470](https://doi.org/10.1371/journal.pone.0143470).
- 674 **Wang P**, Wang H, Gai J, Tian X, Zhang X, Lv Y, Jian Y. Evolution of protein *N*-glycosylation process in Golgi
675 apparatus which shapes diversity of protein *N*-glycan structures in plants, animals and fungi. *Scientific*
676 *Reports*. 2017 Jan; 7:40301. <https://www.nature.com/articles/srep40301>, doi: [10.1038/srep40301](https://doi.org/10.1038/srep40301).

- 677 Wei JH, Seemann J. Golgi ribbon disassembly during mitosis, differentiation and disease progression. Current
678 Opinion in Cell Biology. 2017 Aug; 47:43–51. doi: [10.1016/j.ceb.2017.03.008](https://doi.org/10.1016/j.ceb.2017.03.008).
- 679 Xiang Y, Zhang X, Nix DB, Katoh T, Aoki K, Tiemeyer M, Wang Y. Regulation of protein glycosylation and
680 sorting by the Golgi matrix proteins GRASP55/65. Nature communications. 2013; 4:1659–1659. <https://www.ncbi.nlm.nih.gov/pubmed/23552074>, doi: 10.1038/ncomms2669.
- 682 Yelinek JT, He CY, Warren G. Ultrastructural study of Golgi duplication in Trypanosoma brucei. Traffic (Copen-
683 hagen, Denmark). 2009 Mar; 10(3):300–306. doi: [10.1111/j.1600-0854.2008.00873.x](https://doi.org/10.1111/j.1600-0854.2008.00873.x).

684 Appendix 1

685 DETAILED MODEL

686 General Overview

687 The nomenclature we use in this section is presented in the Tables 1, 2 and 3 in p.15. We
688 propose a coarse-grained, discrete model of the Golgi Apparatus. The smallest element is a
689 vesicle, which defines the unit size of the system. Other compartments are assemblies of
690 fused vesicles; their size is an integer corresponding to an equivalent number of vesicles
691 that have fused to build this compartment. Each unit of membrane is of either *cis*, *medial* or
692 *trans*-identity. A vesicle has a unique identity, and a compartment of size n is a assembly of n
693 discrete membrane patches of different identities.

694 We let the system self-organizes between two boundaries, the ER and the TGN, that are
695 two biological boundaries of the Golgi (**Presley et al., 1997; Klemm et al., 2009**). This theoretical
696 Golgi is self-organized as we do not impose any topological or functional constraints, such
697 as the number of compartments or the directionality of vesicular trafficking. The evolution of
698 the system is only dictated by three mechanisms that are budding, fusion and biochemical
699 conversion (short description in the main text, complete description below). In order to keep
700 the model as simple as possible, we neglect all mechanical and spatial dependencies. This
701 means that we do not take into account motion of compartments in space, or mechanical
702 properties of the membranes. Any two compartments have the possibility to fuse together,
703 with a rate that depends on their relative composition (see below), but not on their size. An
704 alternative model where compartments cannot fuse with one another is presented in App.8
705 on p.42.

706 Biochemical conversion

707 In the Golgi, it is known that cargo (**Kelly, 1985**) and cisternae (**Day et al., 2013**) undergo bio-
708 chemical modifications over time. Changes in membrane identity are driven by maturation
709 cascades of proteins such Rab GTPases (**Suda et al., 2013**). These biochemical conversions
710 can be directly observed using live microscopy, and have been best characterized in the
711 yeast Golgi (**Matsuura-Tokita et al., 2006**). Biochemical conversion of membrane identity
712 is a complex and possibly multi-step process involving different kinds of enzymes. As we
713 are mostly interested in the interplay between biochemical conversion (which mixes differ-
714 ent identities within a single compartment) and sorting mechanisms, we coarse-grain the
715 biochemical conversion events into simple, one step, stochastic processes: *cis*→*medial* and
716 *medial*→*trans*. To simplify the model, we choose the same rate K_m for both conversions.
717 Each patch of membrane (in a vesicle or a compartment, and whatever the surrounding
718 patches are) has the same transition rate.

719 Fusion

Intracellular transport strongly relies on vesicular trafficking (**Takamori et al., 2006**). This involves at least two steps: the budding of a vesicle from a donor compartment (described in the next section), and its fusion with a receiving compartment. The fusion process itself requires close proximity between the receiving compartment and the vesicle, followed by the pairing of fusion actors resulting in membrane fusion. In the current model, the rate of encounter of two compartments is constant, and equal to K_f , while the actual fusion event depends on the biochemical composition of the fusing compartments. *In vivo*, some of the key proteins involved in the fusion process, such as the SNAREs or tethering proteins are known to closely interact with membrane markers like Rab proteins (**Cai et al., 2007**). This is thought to accelerate fusion events between compartments of similar biochemical

727

Manuscript submitted to eLife

728

729

730

731

732

733

734

735

736

737

738

739

740

741

742

743

744

745

746

747

748

749

750

751

752

753

754

755

756

757

758

759

760

761

762

763

764

765

766

767

identities and decrease it between compartments of different identities, a process often called homotypic fusion (*Marra et al., 2007*). To take this into account, fusion is modulated by the probability that both compartments exhibit the same identity at the contact site, corresponding to Eq.1 in the main text.

The fusion rate is maximum (K_f) for two identical compartments, and vanishes between two compartments with no common identity. The exchange of vesicles between compartments of different identities (*Glick and Luini, 2011*), or the fusion of compartments of different identities (*Marsh et al., 2004*), are sometimes regarded as heterotypic fusion. Such processes are allowed within our homotypic fusion model, provided the different compartments share at least some patches of similar identities.

Budding

Budding is the formation of a new vesicles from a large compartment. We assume that each budding vesicle is composed of a single membrane identity, which is consistent with the high specificity of the *in vivo* budding machinery (*Bonifacino and Glick, 2004*). In our model, the flux of vesicles budding from a compartment depends on the size and composition of the compartment. Compartments smaller than 2 cannot bud a vesicle. Compartments of size 2 can split into two vesicles. For larger compartments, we consider a general budding flux for vesicles of identity i (for $i = cis, medial$ and $trans$) of the form:

$$J_{b,i} = K_b \times n \times f(\phi_i) \quad (10)$$

with n the size of the compartment', K_b a constant and $f(\phi_i)$ a function of the composition of the compartment.

One expects the budding flux to follow a Michaelis-Menten kinetics; linear with the number of patches of a given identity ($f(\phi) = \phi$) at small concentration, and saturating to a constant at high concentration (*Vagne and Sens, 2018b*). This scenario is consistent with the fact that budding proteins interact very dynamically with the membrane, attaching and detaching multiple times before budding a vesicle (*Hirschberg et al., 1998*). Previous theoretical works suggest that vesicular sorting of different membrane species is more efficient in the saturated regime (*Dmitrieff and Sens, 2011*). Since one of the main features of the Golgi is to segregate different biochemical species into different compartments, we assume a very high affinity between membrane patches and their budding partners, setting $f(\phi_i) = 1$ if $\phi_i > 0$ and $f(\phi_i = 0) = 0$ (corresponding to Eq.2 of the main text). The budding flux for a given identity thus depends on the total size of the compartment rather than on the amount of that particular identity. This leads to a total budding flux $K_b \times n \times n_{id}$ for a compartment carrying n_{id} different identities. The results of simulations with this linear budding scheme are discussed in App.8 on p.41.

Exits

In cells, the Golgi is placed between two intra-cellular structures that are the ER and the TGN (*Presley et al., 1997; Klemm et al., 2009*). Fluxes of material leaving the Golgi thus include retrograde fluxes toward the ER, carrying immature components such as *cis* and *medial*-Golgi enzymes or recycling ER enzymes, and anterograde fluxes toward the TGN of mature components, such as processed cargo that properly underwent all their post-translational maturation steps (*Boncompain and Perez, 2013*). The exiting fluxes are accounted for by allowing the different compartments in the system to fuse with the boundaries. All compartments, from vesicles to the largest ones, can fuse homotypically with the ER or the TGN to exit the system. Thus, these boundaries are modelled as stable compartments, containing a fraction α_{ER} of *cis* components for the ER and α_{TGN} of *trans* components for the TGN. These

775

Manuscript submitted to eLife

776

777

778

779

780

781

782

783

784

fraction are simply written α when they are assumed to be the same. This allows immature (*cis*) compartments to undergo retrograde exit, and mature (*trans*) components to undergo anterograde exit. In the main text we focus on the case $\alpha = 1$. Lower values of α reduce fusion with the boundaries and increase the residence time of components in the system. This increases the average size of compartments, and increases fluctuations in the system, as large compartments exiting the system induce large fluctuations in the instantaneous size and composition of the system. The impact of α is studied in some details in App.7 p.39.

785

Injection of components

786

Influx to the Golgi

787

788

789

790

791

792

793

794

795

The Golgi receives material from different compartments like the endosomal network, lysosomes, etc... (**Boncompain and Perez, 2013**). As we are primarily interested in characterizing the relationship between the structure and dynamics of the Golgi, and in relating these to the rates of individual biochemical conversion and transport processes, we focus here on the secretory role of the Golgi, and only account for the incoming flux of immature components coming from the ER. We define a rate J of injection of *cis*-vesicles in the system. As the parameters of the system are varied, the injection rate is varied as well in order to keep the total system's size to an almost constant value. This constraint is only approximately enforced using Eq.6, which is only strictly valid when all compartments are pure.

796

797

798

799

800

801

802

803

804

805

806

807

808

809

The impact of the system's size on the structure of the Golgi is shown on Fig.1A of the current appendix. Increasing the total size increases the number of compartments and hence the total fusion flux between compartments. Consequently, compartments are larger in larger systems, and tend to be (slightly) less pure, as fusion increases mixing. In the main text, we restrict ourselves to a system size of $N = 300$. One should remember that Eq. 6, used to predict the system's size N , assumes that compartments are pure (perfectly sorted). Fig.1B - current appendix, shows that this assumption fails to predict N for systems where the budding rate is low compared to the fusion rate (highly interacting compartments). In this regime, compartments have a great probability to fuse together, creating hybrid *cis/medial/trans*-structures. This makes *medial*-patches sensitive to the interaction with the ER and the TGN, and creates an exit flux for these patches that is not observed in a pure regime. Such systems exhibit a larger exit flux and thus a lower N . Note this is only true for biochemical conversion rates lower than the fusion rate, as the system is saturated with *trans*-patches for high k_m (see Eq.4).

810

Transport of passive cargo-proteins

811

812

813

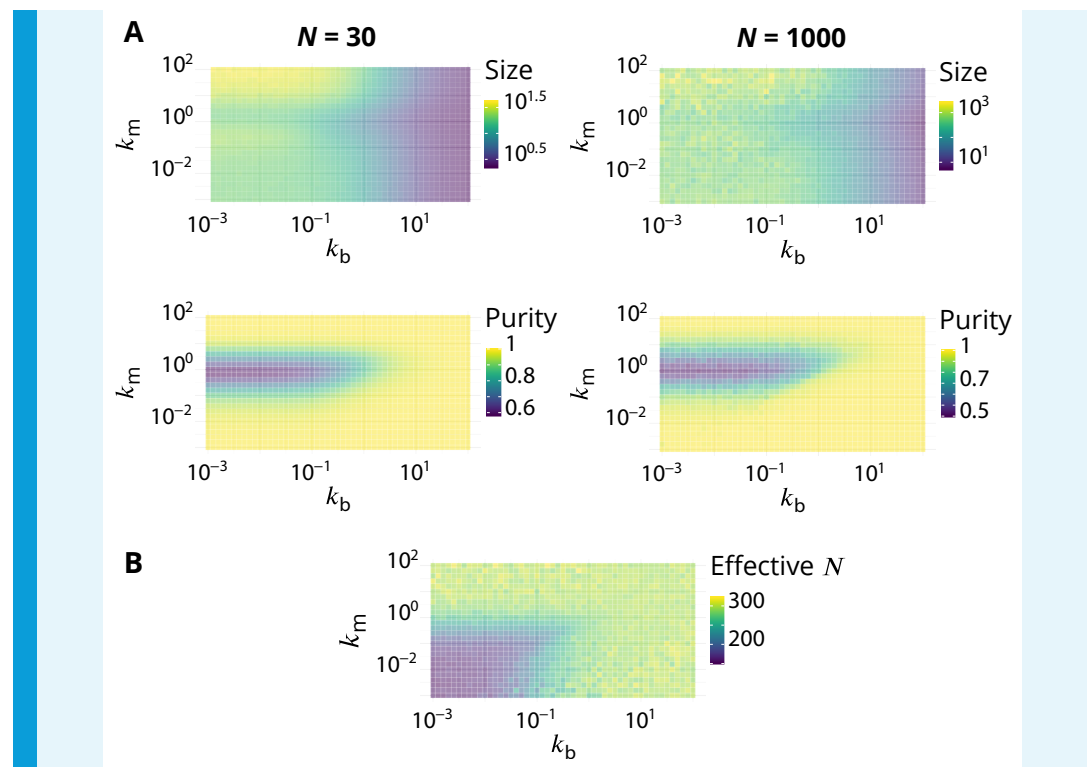
814

815

816

817

The direction of vesicular transport is assessed by following the transport of passive cargo injected from the ER as part of incoming *cis*-vesicles. Cargo molecules are passive in the sense that their probability of joining a vesicle is insensitive to the vesicle membrane identity: when a compartment of size n buds a vesicle, each cargo in this compartment has a probability $1/n$ to join the budding vesicle. In the simulation, the number of cargo molecules in the system is kept to a fixed number (typically 20) by injecting a new one each time one leaves the system through fusion with the boundaries.



818
819
820
821
822
823
824
825
Appendix 1 Figure 1. Link between the total size of the Golgi and its steady-state organisation.
A. Size dependence of the steady-state organisation of the Golgi (to be compared with Fig.2 in the main text). We look at two different systems that only differ in term of the average total size N , that equals 30 or 1000. Typical size of compartments and average system purity are shown as a function of k_m and k_b . In both cases $\alpha = 1$ (see App.1 p.21). B. Average steady-state total size N , as a function of k_m and k_b , for simulation in which the influx is set to have $N \approx 300$ (using Eq.6).

826
827
828
829
830
831
Gillespie algorithm and Software implementation

832
833
834
835
836
837
838
839
840
841
842
843
844
All rates in the system are normalized by the fusion rate: $k_b = K_b/K_f$, $k_m = K_m/K_f$ and $j = J/K_f$. The dynamics of the system can be exactly simulated (to yield the correct trajectories, stochastic noise, etc...) using a Gillespie algorithm ([Gillespie, 1977](#)), also known as stochastic simulation algorithm. After choosing the initial state of the system (see below), the algorithm is implemented as follows:

- 832 1. The rates of all possible events (be it the input of a new vesicle in the system, the
833 fusion between two compartments or between a compartment and one boundary,
834 the budding of a vesicle, or the biochemical conversion of a membrane patch) are
835 calculated. The time interval δt for the next reaction to occur is randomly picked from
836 an exponential distribution with mean $1/R_{TOT}$, where R_{TOT} is the sum of the reaction
837 rates of all possible reactions. The reaction that actually occurs is randomly picked
838 with a probability equal to the rate of this reaction, normalized by R_{TOT} .
- 839 2. The state of the system is modified according to the picked reaction. The rates of all
840 events in the modified system are calculated, and the current time of the simulation is
841 incremented by δt .
- 842 3. The program comes back to step 1 IF the predefined maximum number of iterations
843 has not been reached, AND there is at least one reaction that has a non-zero rate
($R_{TOT} \neq 0$).

844 With the Gillespie algorithm, there is no direct dependency between the number of simulation steps and the actual time that is simulated. The physical time between two consecutive

845

846

847

848

849

850

851

852

853

854

855

856

857

858

859

860

861

862

863

steps decreases with increasing reaction rates. Since we are interested by steady-state quantities, we average over a fixed number of steps rather than a given physical time. As shown in Appendix 4, the steady-state of the system is reached after a physical time of order $1/K_f$. Depending on the parameters, the steady-state is reached after between 10^3 and 10^6 simulation steps. To characterise the steady-state, we disregards the transient regime and data are recorded after 10^6 steps. The full simulation typically last at least 10^7 steps. This arbitrary amount is a good compromise between computation time and the need to accumulate sufficient amount of data to obtain enough statistics on all the measured quantities. In practice, the time needed to reach steady-state can be shortened by starting the simulation from a vesicular system with the predicted amount of *cis*, *medial* and *trans*-species (with Eq.4).

Because simulation steps have different durations, one should be careful when computing time averages. Two different approaches can be used. Either we weight each configuration by the duration between two consecutive time-steps, or we re-sample data to get a fixed time-step between observations, Δt . We checked that both procedures give the same results, and adopted the second approach for the analysis. As the steady-state of the system is reached after a physical time of order $1/K_f$, we take $\Delta t = 1/K_f$.

864 Appendix 2

865 QUANTIFICATION AND STATISTICAL ANALYSIS

866 Computation of the purity

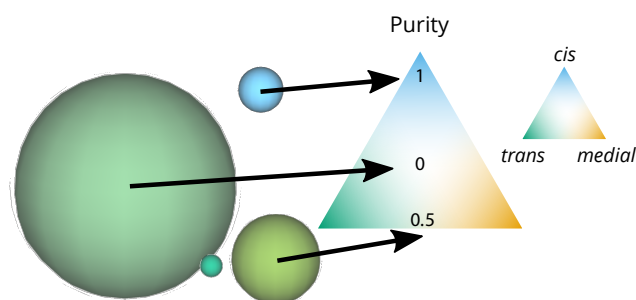
867 The purity of a compartment P is defined such that its value is 0 for a perfectly mixed
868 compartment containing the same amount of *cis*, *medial*, and *trans*-species, and it is equal
869 to 1 for a pure compartment containing a single species. With ϕ_i the fraction of the species i
870 in the compartment, the purity P is defined as:

$$871 \quad P = \sqrt{\frac{3}{2} \sum_i (\phi_i - 1/3)^2} \quad (11)$$

872

873

874 On a triangular composition space where each corner corresponds to a pure compartment,
875 P is the distance from the center of the triangle, see Fig.1 - current appendix. When we
876 show snapshots of the system, each compartment is represented as a sphere whose area is
877 proportional to the compartment size (defined as an equivalent number of vesicles). The
878 composition of a compartment is represented as a color following the color code shown in
879 Fig.1 - current appendix. The purity of the system is a global average (over time and over
880 all compartments) of the purity of individual compartments, weighted by their sizes and
881 ignoring vesicles (that are always pure as they are composed of one unique identity).



882

883 **Appendix 2 Figure 1. Graphical representation of the size and purity of compartments.** Each
884 compartment is represented as a sphere with an area equal to the area of a vesicle (the smallest
885 elements in this snapshot) times the number of vesicles that fused together to create the compartment.
886 The color of the compartment reflects its composition, according to the color code on the triangular
887 composition phase space: 100% *cis* at the top, *medial* at the bottom right, *trans* at the bottom left. The
888 purity of each of these compartments is its distance from a perfectly mixed compartment at the center
889 of the triangle (middle arrow). This distance is normalized so that it equals 1 for a perfectly pure
890 compartment (bottom arrow).

892 Computation of the typical size

893 Among other mechanisms, this theoretical organelle self-organizes by budding and fusion
894 of components. In that sense, it is a scission-aggregation structure which should follow the
895 laws dictating the behavior of this class of systems. One of these laws is the fact that the
896 size distribution for small compartments should follow a power-law. Because of the scission,
897 compartments cannot grow indefinitely and the power-law ends by an exponential cutoff
(Turner et al., 2005; Vagne et al., 2015). Thus, the size distribution c_n of compartments of
size n should, on a first approximation, follow this general formulation:

$$898 \quad c_n \sim \text{Const } n^{-\beta} \exp\left(-\frac{n}{n_c}\right) \quad (12)$$

903 where n_c is the cut-off size and β is an exponent that has been calculated to be $\beta = 3/2$ in a
904 similar system (*Turner et al., 2005*). There are multiple ways to characterize the average size
905 of the distribution, using ratios of moments $k + 1$ over k of the distribution:

$$\langle n \rangle_k \equiv \frac{\sum_{n=1}^{\infty} n^{k+1} c_n}{\sum_{n=1}^{\infty} n^k c_n} \quad (13)$$

909 It turns out that for $n_c \gg 1$, $\sum_{n=1}^{\infty} n^{k-\beta} e^{-n/n_c} \sim 1$ if $1 + k - \beta < 0$ and $\sum_{n=1}^{\infty} n^{k-\beta} e^{-n/n_c} \sim n_c^{1+k-\beta}$
910 if $1 + k - \beta > 0$. In order to have $\langle n \rangle_k \sim n_c$, we need to choose the exponent k such that
911 $k > \beta - 1 = 1/2$ in the present case. In the main text, we adopt $k = 1$ and define the
912 characteristic size of the distribution as:

$$\langle n \rangle \equiv \frac{\sum_{n=1}^{\infty} n^2 c_n}{\sum_{n=1}^{\infty} n c_n} \xrightarrow{n_c \gg 1} \frac{n_c}{2} \quad (14)$$

916 As shown in Fig.2A of the main text, the calculated average is in good agreement with
917 simulations' data.

918 Computation of the mean enrichment

919 To discriminate between the two models of Golgi's dynamics that we can find in the literature,
920 we need to quantify whether the vesicular transport is anterograde or retrograde. Indeed,
921 the "Vesicular transport" model assumes that cargo is transported sequentially from *cis* to
922 *medial* to *trans*-compartments while resident enzymes remain in place, meaning that the
923 vesicular flux is anterograde. On the other hand, "Cisternal maturation" models assume
924 that cargo remain inside cisternae, and resident enzymes are recycled, thus requiring a
925 retrograde vesicular flux. One way to measure this flux in our simulations is to follow passive
926 cargo molecules and quantify whether they move to more or less mature compartments,
927 as they get carried by vesicles. To do so, we record all events that affect cargo molecules.
928 Every time a compartment buds a cargo, we store the composition of this compartment and
929 compare it to the one in which the vesicle later fuses. Both compositions are a vector \vec{C} , with
930 three components that are the fraction ϕ_i (i equals *cis*, *medial* and *trans*) of the donor and
931 acceptor compartments. Defining \vec{C}_d the composition of the donor compartment, and \vec{C}_a
932 the composition of the acceptor, we can compute the enrichment \vec{E} as:

$$\vec{E} = \vec{C}_a - \vec{C}_d \quad (15)$$

933 The sum of both \vec{C} components equals 1 (as they are fractions of each identities), and
934 the sum of \vec{E} components equals $\vec{0}$, which simply means one cannot gain in fraction of
935 any identity without loosing the same amount of the others. We can now compute $\langle \vec{E} \rangle$ to
936 calculate the mean enrichment in *cis*, *medial* and *trans*-species, between a budding event
937 and the next fusion event.

938 However, and because of back fusion events (fusion into the same compartment that
939 previously budded the vesicle), $\langle \vec{E} \rangle$ components can be close to 0. This is particularly true
940 for pure, sorted systems. In that case, a budded vesicle has the same identity as its donor
941 compartment, and thus has a great probability to fuse back with the same compartment or
942 one of very similar composition. That is why, non-treated data do not allow to discriminate
943 well between an anterograde and a retrograde regime when the purity (and thus k_b) is high
944 (Fig.1A - App.6, p.37). As we are primarily interested in the sign of these vectors' components,
945 we normalize \vec{E} using the L_1 norm ($\sum_i |E_i| = 1$).

946 Computation of the vesicular flux vector field

947 The vesicular flux discussed in the previous section can be directly displayed on the triangle
948 of composition we introduced in Fig.1 - current appendix. Instead of computing $\langle \vec{E} \rangle$ for all \vec{E} ,

950

951

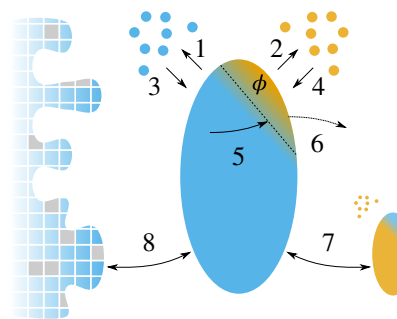
952 we can bin data with respect to the donor compartment composition (typically triangular bins
953 of size $\Delta\phi = 0.1$) and calculate the average enrichment for each bin of donor compartments.
954 To get rid of back fusion effects in this quantification, we remove the vectors \vec{E} for which all
955 components are smaller (in absolute values) than the binning mesh-grid. For each binned
956 composition we can now compute the mean enrichment vector, and plot this vector on
957 the 2D triangular composition space. To emphasize the dominant fluxes in this vector field,
958 the opacity of vectors is set proportionally to the flux of transported cargo per unit time
959 (normalized by the total amount of cargo-proteins in the system). This can be seen on Fig.4 -
960 main text.

961 Appendix 3

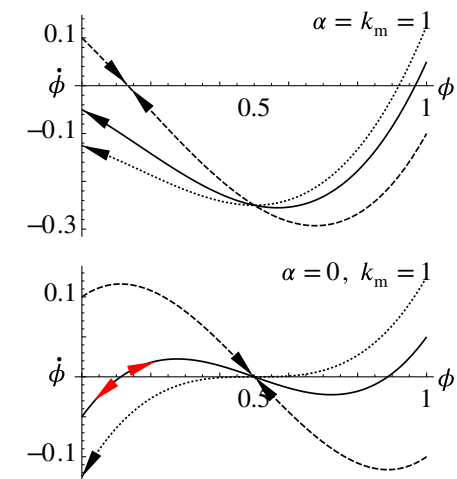
962

ANALYTICAL MODEL FOR THE PURITY OF COMPARTMENTS

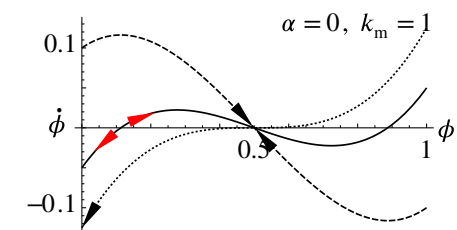
A



B



C



963

964

965

966

967

968

969

970

971

972

973

974

Appendix 3 Figure 1. Analytical description of the *cis*-compartment purity. Related to Fig.2 - main text. A. Analytical model of the steady-state contamination by a *medial*-species (orange) of a *cis*-compartment (blue). The fraction occupied by the *medial*-species is named ϕ . The eight events ((1)-(8)) impacting ϕ are listed in the text. B-C. Time variation $\dot{\phi}$ as a function of ϕ , with $k_m = 1$ and for different k_b (0.9 dashed line, 1.05 solid line, and $1 + 1/8$ dotted line). ϕ has a stable value when $\partial_\phi \dot{\phi} < 0$ and $\dot{\phi}|_{\phi=0} < 0$ (black arrows). It is potentially unstable when $\partial_\phi \dot{\phi} > 0$ and $\dot{\phi}_{\phi \sim 0} = 0$ (red arrows). B. For $\alpha = 1$: $k_b = 0.9$ (dashed) exhibits a stable fixed-point for $\phi > 0$ but with $\phi < 1/2$ as $\alpha > 0$; $k_b = 1.05$ (solid) and $k_b = 1 + 1/8$ (dotted) exhibit a stable concentration for $\phi = 0$. C. For $\alpha = 0$: $k_b = 0.9$ (dashed) exhibits a stable fixed-point for $\phi = 1/2$; $k_b = 1.05$ (solid) exhibits an unstable fixed-point near $\phi = 0$; $k_b = 1 + 1/8$ (dotted) does not display this unstable fixed-point as $k_b \geq k_m + 1/8$ (see text).

975

976

977

978

We want to build a simple model to explain how the purity of the system is affected by the parameters. This is challenging as all events (budding, fusion and biochemical conversion) influence the purity of a compartment. We seek to determine the purity transition, namely the values of k_b and k_m for which a pure system becomes impure.

979

980

981

982

983

984

We make the following approximations, based on the assumption that the system is almost pure: (i) *trans*-compartments are pure as they cannot be contaminated by biochemical conversion. (ii) *cis* and *medial*-compartments share the same purity. (iii) The total amount of the different species N_{cis} , N_{medial} and N_{trans} follows the steady-state repartition of *cis*, *medial* and *trans*-species in a pure limit, given by Eq.4. Most of the components of the system are within compartments.

985

986

987

988

989

The purity of a compartment - defined in the main text - is $P = \sqrt{(3/2 \sum_i (\phi_i - 1/3)^2)}$. We consider that *cis*-compartments (*medial*-compartments) are contaminated by an average fraction $\langle \phi \rangle \ll 1$ of *medial*-patches (*trans*-patches), while *trans*-compartments are pure. The purity of *cis* and *medial*-compartments is thus $P_{cis, medial} = \sqrt{1 - 3\langle \phi \rangle(1 - \langle \phi \rangle)}$ and $P_{trans} = 1$. Weighting these with the fraction of the different species in the system (from Eq.4) gives

990

991

992

$$\langle P \rangle = \frac{2\alpha_{TGN} \sqrt{1 - 3\langle \phi \rangle(1 - \langle \phi \rangle)} + k_m}{2\alpha_{TGN} + k_m} \quad (16)$$

993

994

995

996

To compute the average contamination $\langle \phi \rangle$, we consider the different events that affect the purity of a *cis*-compartment of size n contaminated by a fraction ϕ of *medial*-patches, surrounded by a number n_v of *cis*-vesicles, and a number n'_v of *medial*-vesicles. These events are sketched in Fig.1 - current appendix, and listed below:

1. Budding of *cis*-patches (increases ϕ)
2. Budding of *medial*-patches (decreases ϕ)
3. Fusion of *cis*-vesicles (decreases ϕ)
4. Fusion of *medial*-vesicles (increases ϕ)
5. Conversion of *cis*-patches (increases ϕ)
6. Conversion of *medial*-patches (decreases ϕ)
7. Fusion with a *medial*-compartment ($\phi \rightarrow \frac{1}{2}$)
8. Fusion with the ER ($\phi \rightarrow 0$)

The rate $p(i)$ (normalized by the fusion rate) for each mechanism, and the extent $\delta\phi$ to which it affects ϕ , are:

$$\begin{aligned}
 p(1) &= nk_b, & \delta\phi(1) &= \frac{n\phi}{n-1} - \phi; & p(2) &= nk_b, & \delta\phi(2) &= \frac{n\phi-1}{n-1} - \phi \\
 p(3) &= n_v(1-\phi), & \delta\phi(3) &= \frac{n\phi}{n+1} - \phi; & p(4) &= n'_v\phi, & \delta\phi(4) &= \frac{n\phi+1}{n+1} - \phi \\
 p(5) &= n(1-\phi)k_m, & \delta\phi(5) &= \frac{1}{n}; & p(6) &= n\phi k_m, & \delta\phi(6) &= -\frac{1}{n} \\
 p(7) &= \phi(1-\phi), & \delta\phi(7) &= \frac{1}{2} - \phi; & p(8) &= \alpha(1-\phi), & \delta\phi(8) &= -\phi
 \end{aligned}$$

We can now compute the temporal variation of ϕ : $\dot{\phi} = \sum p(i)\delta\phi(i)$. We concentrate on the limit of large compartments: $n \gg 1$. For simplicity, we also assume that $n \gg (n_v - n'_v)$, so that the net contribution of vesicle fusion to the purity variation, which scales like $(n'_v - n_v)/n$, is negligible. Neglecting stochastic fluctuations, the mean-field evolution of the fraction of contaminating species is:

$$\dot{\phi} = (k_m - k_b)(1 - 2\phi) + \phi(1 - \phi)(1/2 - \phi - \alpha) \quad (17)$$

Below, we discuss separately the case where $\alpha = 1$ (fast fusion with the ER boundary - discussed in the main text), and the case where $\alpha = 0$ (no exit through the ER - discussed in App.7, p.39).

• $\alpha = 1$. A pure compartment; $\phi = 0$, is stable ($\dot{\phi}|_{\phi=0} < 0$) when $k_m < k_b$. If $k_m > k_b$, the compartment is contaminated by a stable fraction of *medial*-patches given by the single stable root of Eq.17 (see Fig.1B - current appendix). The purity transition lines shown in Fig.2C of the main text are obtained by inserting this root in Eq.16.

• $\alpha = 0$. If $k_b < k_m$, the single root of Eq.17 is for $\phi = 1/2$ and is stable. The system is always impure with mixed *cis-medial* compartments. If $k_b > k_m$, pure compartments ($\phi = 0$) are stable at the mean-field level, but there exist an unstable fixed point for small values of ϕ . Stochastic fluctuations may bring the system passed the unstable fixed point toward the stable mixed solution $\phi = 1/2$. For $k_b > k_m + \frac{1}{8}$, $\phi = 1/2$ is an unstable fixed point and the only stable solution is for $\phi = 0$ (see Fig.1C - current appendix). The purity transition is thus with the range $k_m < k_b < k_m + \frac{1}{8}$.

A more precise characterization of the transition in the case $k_b > k_m$ requires to include stochastic effects. The different stochastic events are associated to very different fluctuations amplitudes. Budding and fusion of vesicles and biochemical conversion of membrane patches represent small fluctuations for a large compartment, while fusion between compartments and with the boundaries represent a very large alteration of the purity. In what follows, we propose a simplified treatment of this process, focusing on the case $\alpha = 0$ for simplicity, and neglecting the contribution of vesicle fusion as discussed above. For a compartment of size n contaminated by n_{medial} patches, we identify 2 types of mechanisms (depending on their amplitude). First, a smooth drift in the contamination due to biochemical conversion (with a rate $k_m * (n - n_{medial})$) and budding (with a rate $k_b n$). Second, a jump in the contamination due to fusion with the neighbor compartment (rate $n_{medial}(n - n_{medial})/n^2$). We compute below the mean contamination, assuming that the *cis*-compartment spends a

1033

1034

1035

1036

1037

1038

1039

time τ_{conta} undergoing small fluctuations $\delta\phi \simeq 0$ close to the pure state, before fusing with a *medial*-compartment of composition $1 - \delta\phi$. The resulting compartment with $\phi \simeq 1/2$ then spends a time τ_{deconta} undergoing a decontamination process, which depends on the balance between budding and biochemical conversion.

1040

1041

We first calculate the average value $\delta\phi$ of the contamination around $\phi = 0$ due to biochemical conversion and budding, disregarding inter-compartment fusion. The probability $\mathbb{P}(n_{\text{medial}})$ of finding n_{medial} in the cisterna satisfies:

1042

1043

1044

1045

1046

1047

$$\begin{aligned} \dot{\mathbb{P}}(n_{\text{medial}}) &= -\mathbb{P}(n_{\text{medial}})(k_m(n - n_{\text{medial}}) + k_b \times n) \\ &\quad + \mathbb{P}(n_{\text{medial}} - 1) k_m(n - n_{\text{medial}} + 1) \\ &\quad + \mathbb{P}(n_{\text{medial}} + 1) k_b \times n \end{aligned} \quad (18)$$

In the limit $n \gg n_{\text{medial}}$, this becomes:

1048

1049

1050

$$\dot{\mathbb{P}}(n_{\text{medial}})/n = -\mathbb{P}(n_{\text{medial}})(k_m + k_b) + \mathbb{P}(n_{\text{medial}} - 1)k_m + \mathbb{P}(n_{\text{medial}} + 1)k_b \quad (19)$$

The steady-state solution is

1051

1052

1053

$$\mathbb{P}(n_{\text{medial}}) = (k_m/k_b)^{(n_{\text{medial}})} / \sum_{i=0}^{n/2} (k_m/k_b)^i = \frac{(k_b - k_m)(k_m/k_b)^{(n_{\text{medial}})}}{k_b - k_m(k_m/k_b)^{n/2}} \quad (20)$$

1054

and the average contamination $\delta\phi$ due to budding and biochemical conversion is:

1055

1056

1057

$$\delta\phi = \sum_{i=0}^{n/2} \frac{i}{n} \times \mathbb{P}(i) \simeq \frac{k_m}{n(k_b - k_m)}, \text{ (for } k_b > k_m \text{)} \quad (21)$$

1058

1059

1060

These fluctuations in composition allow fusion between compartments, at a rate $\delta\phi(1 - \delta\phi) \simeq \delta\phi$ (for $\delta\phi \ll 1$). The average waiting time for an inter-compartment fusion event is thus $\tau_{\text{conta}} = 1/\delta\phi$.

1063

1064

1065

1066

1067

After inter-compartment fusion, the compartment is at $\phi = 1/2$, which is an unstable fixed point according to Eq.17. Any small fluctuation in composition leads to a smooth decontamination that satisfies $\dot{\phi} = (k_m - k_b)(1 - 2\phi)$, disregarding inter-compartment fusion. The decontamination time τ_{deconta} and the average contamination during the process $\langle\phi\rangle_{\text{deconta}}$, can be estimated by integrating $\dot{\phi}$, from $\phi = 1/2 - 1/n$ to $\phi = 0$:

1068

1069

1070

$$\tau_{\text{deconta}} = \frac{\log(n/2)}{2(k_b - k_m)}, \quad \langle\phi\rangle_{\text{deconta}} = \frac{2 + n [\log(n/2) - 1]}{2n \log(n/2)} \quad (22)$$

1071

We can now calculate $\langle\phi\rangle$ as a temporal average of ϕ :

1072

1073

1074

1075

1076

1077

1078

1079

1080

1081

1082

1083

1084

1085

$$\langle\phi\rangle = \frac{\tau_{\text{conta}} \times \delta\phi + \tau_{\text{deconta}} \times \langle\phi\rangle_{\text{deconta}}}{\tau_{\text{conta}} + \tau_{\text{deconta}}} \quad (23)$$

When $\log(n/2)$ is close to 1 (typically true for the range of n that is interesting here, $n \sim 100$), $\langle\phi\rangle$ can be simplified to:

$$\langle\phi\rangle \simeq \frac{k_m + 2k_m(k_b - k_m)}{2k_m + 2n(k_b - k_m)^2} \quad (24)$$

Injecting this result into Eq.16 gives the approximate purity boundary for $\alpha_{\text{ER}} = 0$:

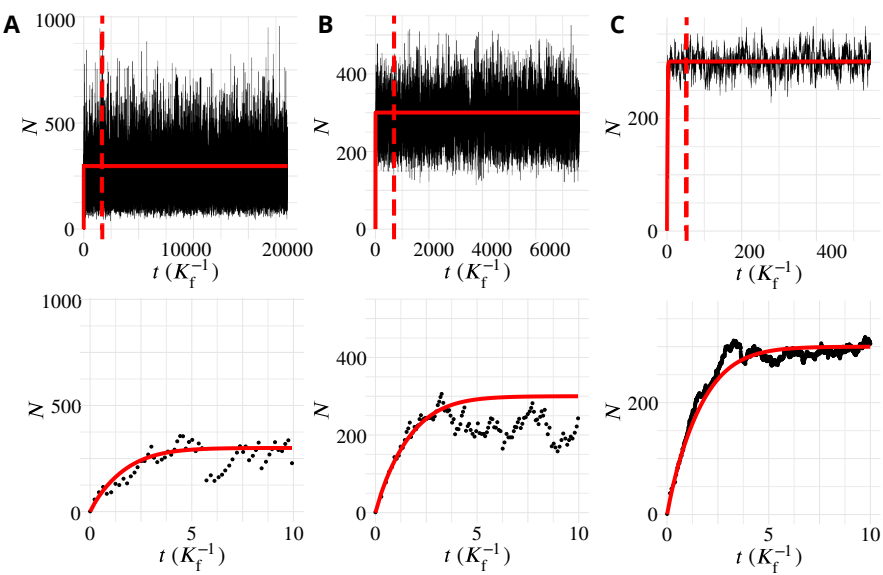
$$\langle P \rangle \simeq 1 - \frac{3\alpha_{\text{TGN}}}{2\alpha_{\text{TGN}} + k_m} \frac{k_m + 2k_m(k_b - k_m)}{2k_m + 2n(k_b - k_m)^2} \quad (25)$$

Despite numerous simplifications, the model gives good predictions on the purity, both for $\alpha_{\text{ER}} = \alpha_{\text{TGN}} = 1$ (Fig.2 - main text) and for $\alpha_{\text{ER}} = 0, \alpha_{\text{TGN}} = 1$ (Fig.1 - App.7, p.39). Depending on the normalized biochemical conversion rate k_m , we can discriminate three regions in the purity phase diagram:

- 1086 • $k_m \gg 1$, the system is saturated in *trans*-species and is thus always pure.
- 1087 • $k_m \sim 1$, compartment's contamination occurs by biochemical conversion, matured
- 1088 species are sorted by budding. The purity transition occurs for $k_b \simeq k_m$ (compartments
- 1089 are impure system if $k_b < k_m$).
- 1090 • $k_m \ll 1$, the system is saturated by *cis* and *medial*-compartments, and the transition of
- 1091 purity occurs for $k_b \ll 1$: the fusion rate is dominant in this regime. Thus interaction
- 1092 with the boundaries or other compartments are crucial to understand the transition of
- 1093 purity. For $\alpha_{ER} = 1$, fusion with the ER decontaminates the system, thus the transition
- 1094 occurs for $k_b < k_m$. The transition becomes independent of k_b for very small biochemical
- 1095 conversion rates, where the system is saturated in *cis*-species. For $\alpha_{ER} = 0$, purifying
- 1096 the system by recycling compartments is not possible, and inter-compartment fusion
- 1097 decreases the purity, thus the transition of purity requires large values of the budding
- 1098 rate $k_b > k_m$, as given by Eq.25.

1099 **Appendix 4**

1100 **DE NOVO FORMATION AND CARGO EXPORT KINETICS**



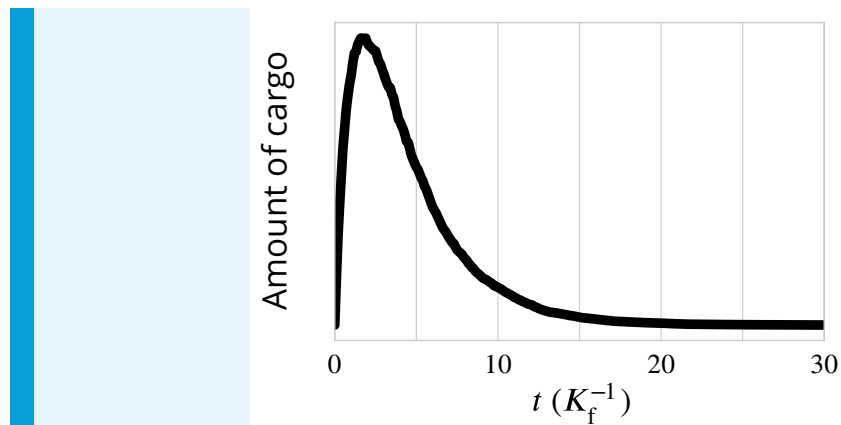
1101
1102 **Appendix 4 Figure 1. Transient regime towards the steady-state** System's size (total number of
1103 membrane patches in the system) as a function of time (in unit $1/K_f$) for three different values of the
1104 budding rate (A: $k_b = 10^{-2}$, B: $k_b = 1$, C: $k_b = 10^2$). The top row shows the full simulations, with a vertical
1105 dashed bar when the number of simulation steps reaches 10^6 . The steady-state data analysed and
1106 discussed in this paper are recorded after this time, and the full simulation typically lasted 10^7
1107 time-steps. The bottom row shows the evolution at early time (de-novo formation). The red lines are the
1108 analytical solution given by Appendix 4 Eq.3.

1109 **Transient evolution toward the steady-state: De novo formation**

1110 The evolution of the system's size with time for different values of the dimensionless budding
1111 rate k_b is shown in Fig.1 - current appendix. The organelle forms de-novo, and reaches
1112 the steady-state after a time of order a few $1/K_f$. The steady-state is reached under any
1113 parameter values, but the fluctuations around the steady-state depend on the parameter, as
1114 discussed in Appendix 5. The analytic calculation presented in Eqs.3 (red line in Fig.1 above)
1115 is very accurate for high budding rate, but gives a 10% error for low budding rate.
1116

1117 **Transit kinetics of passive cargo.**

1118 The cargo used as marker of vesicular transport directionality can be used to quantify the
1119 transit kinetics of a passive cargo across the self-organised organelle. Fig.2 - current appendix
1120 shows the amount of cargo present in the system as a function of time during a typical
1121 "pulse-chase" experiment, in which a given number of cargo molecules is allowed to exit
1122 the E.R. at $t = 0$, by joining the vesicles constituting the influx j . The amount of cargo in
1123 the system initially increases, then decreases in a close-to-exponential fashion. The export
1124 kinetics resemble the one observed by iFRAP (Fig.2 i of **Patterson et al. (2008)**) or using the
1125 RUSH technics (Fig.3 e of **Boncompain et al. (2012)**).



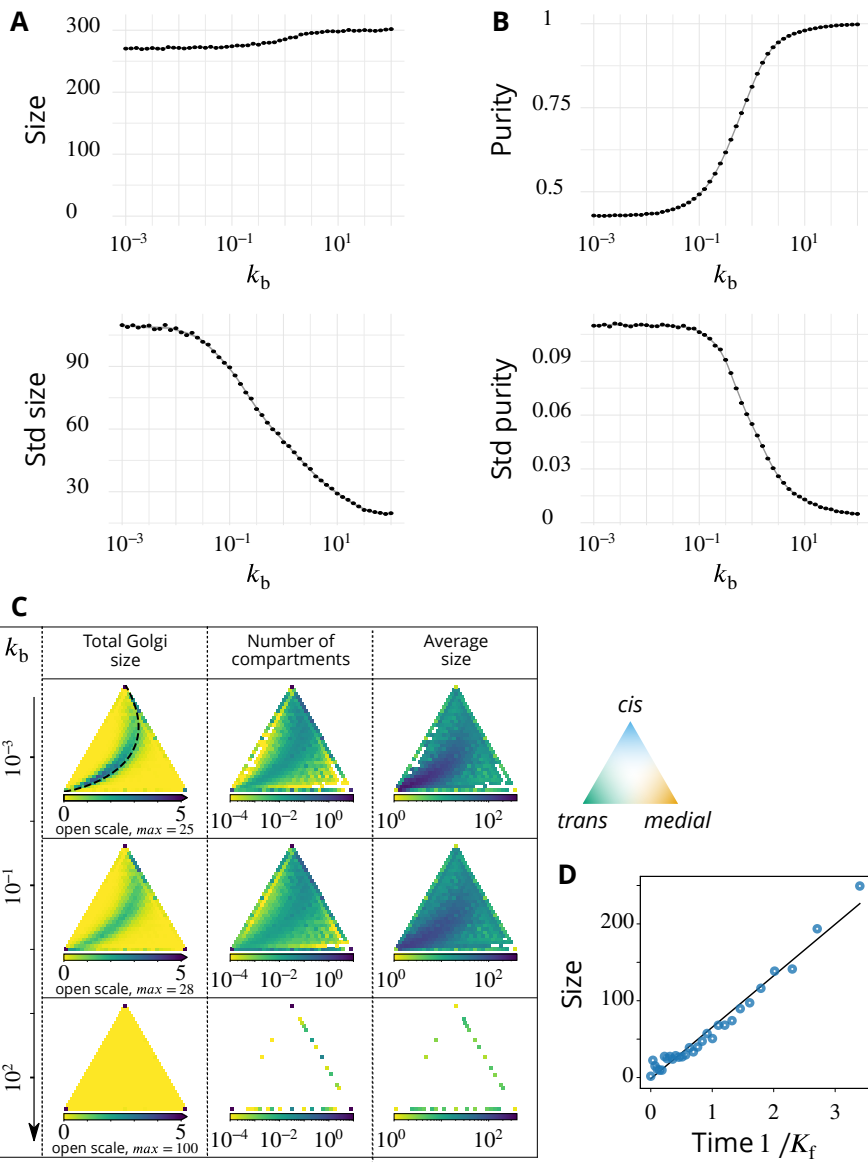
1126
1127
1128
1129
1130
1131
1132
1133
1134
1135

Appendix 4 Figure 2. Exit kinetics of passive cargo. Simulated amount of cargo in the Golgi following a pulse-chase like simulation in which 1000 cargo molecules are trapped in the ER and allowed to be packaged into ER exiting vesicles at $t = 0$. This is expected to mimick the iFRAP experimental setup used in **Patterson et al. (2008)** and to the RUSH setup used in **Boncompain et al. (2012)**. The decay of the amount of cargo is close to a single-time exponential decay, in agreement with experimental observations for transiting cargo (Fig.2 i of **Patterson et al. (2008)** and Fig.3 e in **Boncompain et al. (2012)**). Parameters are $k_b = k_m = \alpha = 1$, corresponding to the “sorted regime” (the triangle of Fig.2) which we expect to be the most reasonable for mammalian Golgi.

1136 **Appendix 5**

1137

DETAILED organisation



1138

1139
1140
1141
1142
1143
1144
1145
1146
1147
1148
1149
1150

Appendix 5 Figure 1. Steady-state composition and fluctuation of compartments. Related to Fig.2 - main text. (A-B) Characterization of the temporal fluctuations of the system as a function of the budding rate k_b . A. average values of the system total size (top panel) and standard deviation of the size (bottom panel). B. average values of the system purity (top panel) and standard deviation of the purity (bottom panel). C. Distribution of the total size, number of compartments and their average size, as a function of the composition of the compartments, shown in a triangle plot (see App.2) for different values of the (normalized) budding rate k_b . The average size for a given composition is calculated as the average size divided by the average number of compartments. Plots are shown for four different values of k_b , with $k_m = \alpha = 1$. The dashed black line on the top, left panel (low k_b regime) corresponds to the theoretical prediction of Eq.9. D. The evolution of the compartment's size as a function of time, in the low $k_b = 10^{-3}$ limit, agrees with the linear prediction of Eq.7

The fluctuations of the system around its steady-state are characterized by computing the temporal standard deviation of the total system's size and purity, shown in Fig.1A-B - current appendix. Fluctuations decrease as the budding rate k_b increases, owing to the

1151

Manuscript submitted to eLife

1152

1153

1154

1155

1156

1157

1158

1159

1160

1161

1162

1163

1164

1165

1166

1167

1168

1169

1170

1171

1172

1173

1174

1175

1176

1177

1178

1179

1180

fact that compartments are on average smaller for larger budding rate, so that the removal of a compartment by fusion with the boundaries has a smaller impact on the state of the system. We note in Fig.1A - current appendix, that the total size of the system depends on the budding rate k_b , despite the fact that the influx j is varied according to Eq.6 to limit variations of the system's size. This is due to the fact that Eq.6 is valid only in the limit of pure compartments (large k_b). For smaller values of the budding rate, *medial*-compartments contaminated by *cis* and *trans*-species and may thus exit the system by fusing with the boundaries, which decreases the total size for low k_b . For the regime we are interested in, namely $k_m \sim \alpha \sim 1$, this phenomenon is practically negligible, but its impact on the average size is more severe for lower k_m (App.1, p.23).

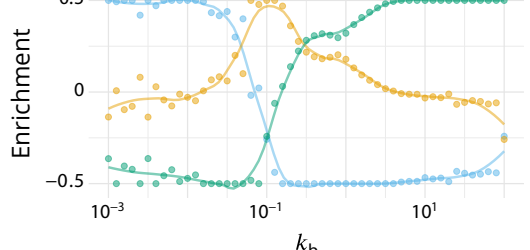
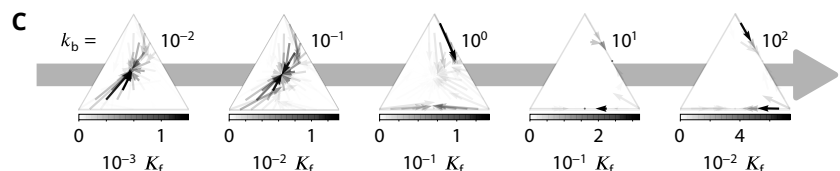
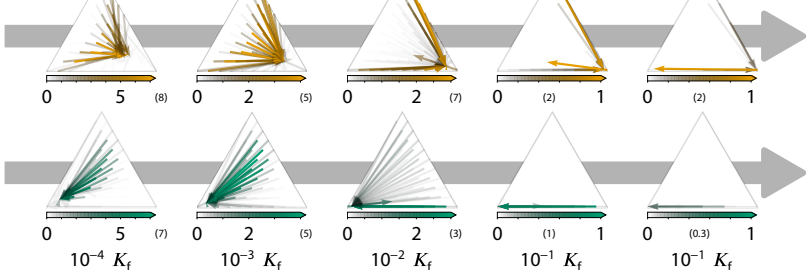
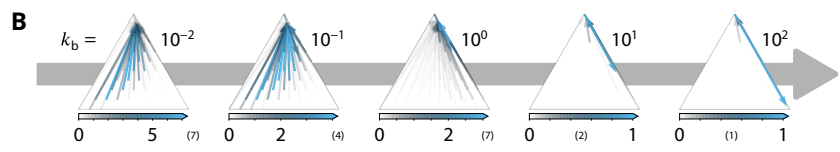
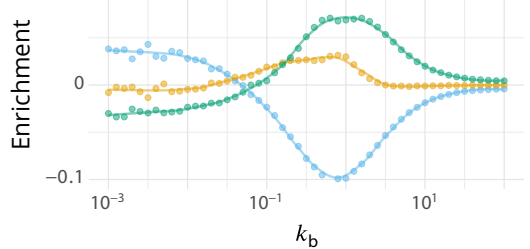
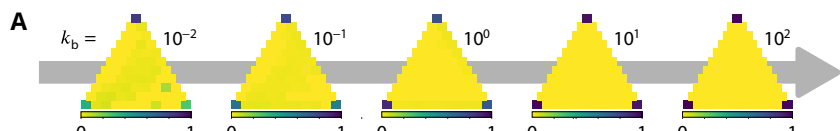
We also characterize the variation of the size of compartments and their abundance as a function of their composition. In the main text (Fig.4), variations of the total size (number of membrane patches) and the number of compartments is shown as a function of their composition, in the composition triangular space defined in App.2, p.25. This is obtained by binning the composition space in such a way that the characterization is both relatively precise and statistically significant (binning ϕ with a mesh of 1/30). The size and number of compartments are averaged over the simulation time (once the steady-state is reached) for each composition bin. These results are reproduced in Fig.1C - current appendix, where the average size of compartment, computed as the ratio of average size over average number of compartments, is also shown.

For low values of the budding rate k_b , both the size and the number of compartments follow the theoretical line obtained from the "cisternal maturation" limit (Eq.9). Compartments also grow linearly in time, in agreement with the linear prediction of Eq.7. Their sizes are shown in Fig.1D - current appendix, as a function of their theoretical lifetime. The sizes are computed by measuring the average compartment size for each composition bin along the theoretical line. The compositions are then used to estimate the lifetime of compartments using Eq.9.

1181 Appendix 6

1182

DETAILED CHARACTERIZATION OF VESICULAR TRANSPORT



1183

1184
1185
1186
1187
1188
1189
1190
1191
1192
1193
1194
1195
1196
1197
1198
1199

Appendix 6 Figure 1. Detailed characterizations of the vesicular transport. Related to Fig.3-4 - main text. $\alpha = k_m = 1$ for all panels. A. **Characterization of vesicle back-fusion** (fusion of vesicles with the same compartment or with a compartment of comparable composition). Top panel: fraction of vesicular flux undergoing back-fusion, as a function of the composition of the budding compartments, for different values of the budding rate k_b . Bottom panel: non-normalized enrichment in *cis* (blue), *medial* (orange) and *trans*-species (green) seen by a passive cargo, between a budding and the next fusion event, as a function of k_b . B. **Vesicular fluxes of *cis* (blue), *medial* (orange) and *trans* (green) vesicles** for different values of the budding rate k_b . The base of each arrow gives the composition of the donor compartment and the tip gives the average composition of receiving compartments - ignoring back-fusion - as in Fig.4, main text. The opacity of the arrows represents the normalized number of cargo (divided by the total number of cargo in the system) transported per unit time (normalized by the fusion rate). C. **Net vesicular flux, excluding vesicle biochemical conversion**, for different values of the budding rate k_b . Top panel: vesicular flux is represented as a vector field as in Fig.4, main text. Bottom panel: vesicular flux is represented as the enrichment between the donor and the acceptor compartment, excluding back-fusion, as in Fig.3, main text.

1200
1201
1202
1203
1204

Quantification of the back-fusion

In the main text, we discussed the importance of back-fusion when the budding rate k_b increases. To determine the likelihood of a vesicle to fuse back with the compartment it budded from, or a compartment of similar composition, we analyzed the trajectories of passive cargo-proteins.

1205
1206
1207
1208
1209
1210
1211
1212
1213
1214

Back fusion is defined as a vesicular transport event where the donor and acceptor compartments fall within the same composition bin. The fraction of the total vesicular flux leaving a compartment that undergoes back fusion is shown as a function of the composition of compartments in a triangular composition space in Fig.1A (top panel) - current appendix. As expected, back-fusion is dominant near the vertices of the composition triangle, where compartments are pure and mostly bud vesicles of identity similar to their own identity. These vesicles are very likely to fuse back with the donor compartment by homotypic fusion. The back fusion flux increases with the budding rate k_b , going from ~ [90%, 10%, 20%] for respectively [*cis*, *medial* and *trans*]-compartments when $k_b = 10^{-2}$, to ~ 100% when $k_b = 10^2$ for all compartments.

1215
1216
1217
1218
1219
1220
1221

The mean enrichment (composition difference between donor and acceptor compartments) seen by a transport vesicle is plotted in the main text in a normalized fashion. The non-normalized enrichment is plotted in Fig.1A (bottom panel) - current appendix. The mean enrichment for all three identities vanishes when k_b is large. This is explained by the contribution of back fusion. When k_b is large, the compartments are very pure, and vesicles have a high probability to undergo back fusion, leading to a small value of the net enrichment.

1222
1223
1224
1225
1226
1227
1228
1229
1230

Vesicular transport by composition

Fig.4 of the main text shows the average flux of vesicular transport as a vector field on the triangular composition phase space. The main conclusion is that the vesicular flux is retrograde (toward *cis*-compartments), when the compartments are mixed (low budding rate k_b), anterograde when the compartments are pure (high k_b), and centripetal (toward compartments of *medial*-identity) for intermediate budding rates. In the main text, only the total flux is described, which is the sum of the fluxes of vesicles of the three different identities. To better understand this net enrichment, the total flux can be dissected into the flux of *cis*, *medial* and *trans*-vesicles. These results are shown in Fig.1B - current appendix.

For low budding rate ($k_b \ll 1$), compartments are mixed with all three identities, with a composition distributed around a trajectory given by Eq.9 and shown in Fig.1C - current appendix. These mixed compartments emit vesicles of all identities. The *cis*-vesicles predominantly fuse with pure *cis*-compartments, which always exist at steady-state, since pure

1232

Manuscript submitted to eLife

1233

1234

1235

1236

1237

1238

1239

1240

1241

1242

1243

1244

1245

1246

1247

1248

1249

1250

1251

1252

1253

1254

1255

1256

1257

1258

1259

1260

1261

1262

1263

1264

1265

1266

1267

1268

1269

1270

1271

1272

1273

1274

1275

1276

1277

1278

cis-vesicles are continuously being injected in the system. On the other hand, *medial* and *trans*-vesicles fuse with *cis/medial* and *cis/trans*-compartments, as pure *medial*-compartments are absent, and pure *trans*-compartments are few and transitory. In this limit, the net enrichment is completely dominated by the retrograde transport of *cis*-vesicles, and is positive in *cis*-identity and negative in *trans*-identity.

For intermediate budding rate ($k_b \sim 0.1 \rightarrow 1$), and as k_b increases, components can be efficiently sorted as they mature, since the budding and biochemical conversion rates are of the same order. Medial compartments are rather unstable, as they can fuse with both *cis*-rich and *trans*-rich compartments. Their reformation involves *medial* vesicles leaving *cis*-rich and *trans*-rich compartments to fuse with each other or small *medial*-rich compartments. Fig.1C - current appendix, shows that this is the main contribution to the overall vesicular flux, thereby defining the centripetal net vesicular flux shown in Fig.4 - main text. Note that they primarily exit *trans*-compartments for $k_b \sim 0.1$, and *cis*-compartments for $k_b \sim 1$, denoting a transition from retrograde to anterograde vesicular fluxes.

For high budding rate ($k_b \gg 1$), compartments are very pure, and most budding events lead to vesicle back fusion from the donor compartment (Fig.1A - current appendix). A new phenomenon can be observed, which is the anterograde transport of *cis* and *medial*-vesicles fusing with *medial* and *trans*-compartments, respectively. This is due to vesicle biochemical conversion *after* budding, as discussed below.

Role of vesicles biochemical conversion

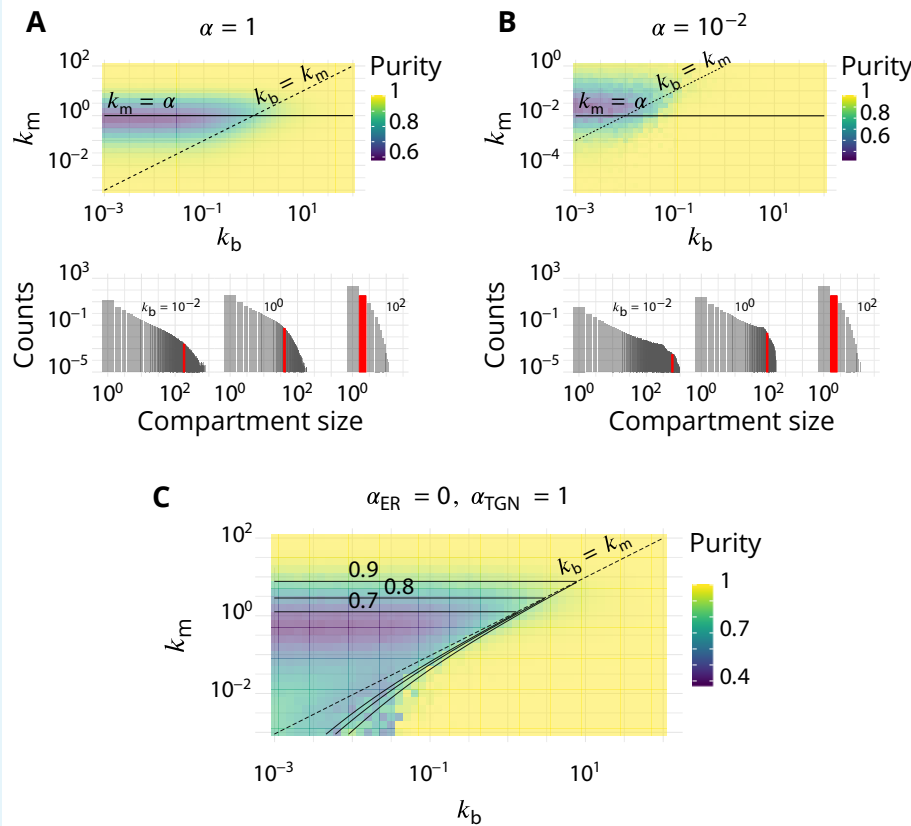
The biochemical conversion of vesicles after their budding from an immature compartment has been presented as a mechanism to prevent back fusion with the donor compartment and to promote anterograde vesicular transport (see Discussion - main text). This mechanism is naturally included in our model, as vesicles have the same biochemical conversion rate than any membrane patch that belong to bigger compartments. One can notice on Fig.1B - current appendix, that there is a major increase of the anterograde *cis*-to-*medial* and *medial*-to-*trans* vesicular fluxes between $k_b = 10$ and $k_b = 10^2$. This is due to the biochemical conversion of the vesicles *after* their budding. The budding vesicle has the same identity than the donor compartment, but undergoes biochemical conversion before undergoing back fusion and fuses with a more mature compartment.

Fig.1C - current appendix, shows the net vesicular flux (for the same simulation than in the main text) ignoring the events where vesicles undergo biochemical conversion after their budding. The net vesicular flux vanishes in the vector field for high budding rates when these events are removed. We interpret this result considering dimers and trimers are dominant when k_b is large. Disregarding vesicle biochemical conversion, such compartments emit as many immature vesicles fusing with immature compartments as mature vesicles fusing with mature compartments, yielding a vanishing net vesicular flux. However, this is not true for the net enrichment which still displays an anterograde signature of the vesicular transport. Indeed, the explanation of the vesicular transport considering the minority identity (see Discussion section in the main text) is still relevant in this regime; compartments larger than 3 vesicles can generate an anterograde transport by budding patches of membrane that just underwent biochemical conversion. Consequently, the net enrichment displays the characteristics of an anterograde vesicular flux even in the absence of vesicle biochemical conversion.

1279 Appendix 7

1280

BOUNDARIES COMPOSITION



Appendix 7 Figure 1. Impact of the composition of the boundaries of the system (ER and TGN) on the steady-state organisation. Related to Fig.2 - main text. (A-B). The fraction α of active species driving homotypic fusion with the boundaries are identical for the ER and the TGN. A. $\alpha = 1$ (same value as in the main text) B. $\alpha = 10^{-2}$. For both cases, the top panel is the purity diagram as a function of the normalized biochemical conversion rate k_m and budding rate k_b . Dashed lines correspond to $k_m = k_b$ and solid lines to $k_m = \alpha$. For both cases, the bottom panel shows some examples of the size distribution for $k_m = \alpha$ and different values of k_b . C. Purity diagram as a function of k_m and k_b when fusion with the ER is abolished: $\alpha_{ER} = 0$ whereas $\alpha_{TGN} = 1$. Solid lines are the predictions of the analytical model developed in App.3.

Our system contains two boundaries: the *cis* face (the ER) and the *trans* face (the TGN). *cis* vesicles are injected via the *cis* face, and compartments may exit the system by fusing with either boundary. The way the different compartments fuse with the boundaries has a strong impact on their lifetime and average size. In the model, this is characterized by the parameter α , which represents the fraction of the boundary composed of species able to elicit homotypic fusion of Golgi's components, *i.e.* the fraction of *cis* species in the ER and of *trans* species in the TGN, and might be different for the two boundaries. In the main text, we focus on the case $\alpha = 1$ (arguably the maximum possible value) for both *cis* and *trans* boundaries. Here, we discuss the impact of this parameter on the structure of the steady-state, and we compare the results of simulations with the analytical model derived in App.3.

Decreasing this parameter has two major impacts on the steady-state organisation: it decreases the biochemical conversion rate for which the steady-state fraction in *cis*, *medial* and *trans*-species are equal and it increases the residence time of compartments in the

1303

Manuscript submitted to eLife

1304

1305

1306

1307

1308

1309

1310

1311

1312

1313

1314

1315

1316

1317

1318

1319

1320

1321

1322

1323

1324

1325

1326

1327

1328

1329

1330

1331

1332

1333

1334

1335

1336

1337

1338

1339

1340

1341

1342

1343

1344

1345

1346

1347

system. This increases their size, as they have more time to aggregate, and increases the fluctuations in the system, as larger compartments have a stronger impact each time they exit or fuse together.

The impact of α on the fraction of *cis*, *medial* and *trans*-species in the system is rather straightforward if compartments are pure (Eq.4). In this case, the exit flux can be exactly computed, and Eq.4 shows that the different species are in equal amount at steady-state when $k_m = \alpha$. If $k_m \gg \alpha$, the membrane patches have time to undergo biochemical conversion before exiting the system, which is then dominated by *trans*-species. The purity of the compartment is high, but this is a rather uninteresting limit as the system is dominated by a single species. If $k_m \ll \alpha$, compartments are recycled out of the system before *trans*-membrane patches appear, and the system is dominated by *cis* and *medial*-species, which are of equal amount at steady state if the system is perfectly sorted.

The same conclusion can be reached in the slow budding regime when compartments are not pure. Let's consider a *cis*-rich compartment of size n contaminated by a fraction ϕ_{medial} of *medial*-species, and let's disregard, for simplicity, budding and fusion with other compartments. The number of *medial*-patches increases by biochemical conversion with a flux $k_m n(1 - \phi_{\text{medial}})$, and decreases by compartment fusion with the boundary, which removes all *medial*-patches with an average flux $\alpha(1 - \phi_{\text{medial}}) \times n \phi_{\text{medial}}$. At steady-state, one thus expects $\phi_{\text{medial}} \simeq k_m / \alpha$, suggesting that the lowest purity will be observed for $k_m \simeq \alpha$. The results of simulations, shown in Fig.1A-B - current appendix, confirm this prediction.

The transition of purity occurs when sorting mechanisms become more efficient than mixing mechanisms. As a first approximation mixing occurs by biochemical conversion and sorting by budding, yielding the prediction that the purity transition occurs when $k_b \simeq k_m$. Additional mixing mechanisms include the fusion of two slightly impure compartments of different compositions. Such slow events become relevant if compartments remain in the system for a long time, *i.e.* if fusion with the boundaries is slow (small values of α). In this case, the transition of purity occurs for $k_b > k_m$. Phase diagram of the purity of the system for a system where $\alpha = 10^{-2}$ can be found in Fig.1B - current appendix. As expected the diagram is centered around $k_m = \alpha$, with a transition of purity between $k_b \sim 10^{-2}$ and $k_b \sim 10^{-1}$ (and thus $k_b > k_m$).

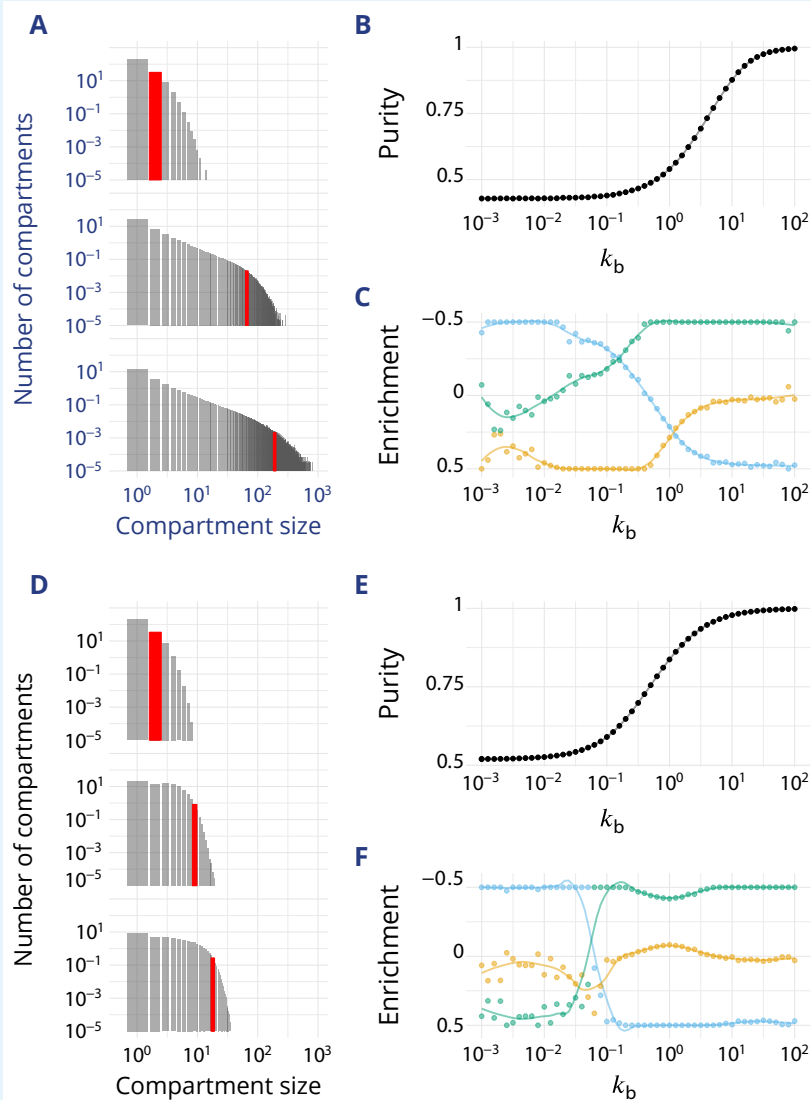
As it tunes the residing time of compartments in the system, α also impact the average size of compartments. Decreasing the value of α increases the residence time and leads to larger compartments, as predicted by Eq.4. Note however that for small budding rates, when compartments are mixed and their exit through the boundary is difficult to estimate, the size distribution deviates from the single-component ideal distribution.

The Golgi being a highly polarized organelle, it could be argued that the parameters controlling the fusion with the *cis* face (ER) and the *trans* face (TGN), α_{ER} and α_{TGN} could be different. An obvious way to reduce the retrograde exit of material from the ER is to reduce α_{ER} . To investigate the role of this asymmetry, we use an extreme regime of $\alpha_{\text{ER}} = 0$ and $\alpha_{\text{TGN}} = 1$. This prevents the recycling of impure compartments by fusion with the ER and broadens the low purity region of the parameter space, as shown in Fig.1C - current appendix, and explained by the analytical model presented in App.3

Appendix 8

1348

OTHER BUDDING/FUSION SCHEMES



1350

1351

1352

1353

1354

1355

1356

1357

1358

Appendix 8 Figure 1. Impact of different budding and fusion kernels on the system's organisation and vesicular transport. Related to Fig.2-3-4 - main text. $k_m = \alpha = 1$. (A-C): Linear budding scheme. (D-F): Inter-compartment fusion is prohibited. A and D: Size distribution of compartment for k_b equals 10^{-2} (top), 1 (middle) and 10^2 (bottom). B and E: Steady-state purity as a function of k_b . C and F: Enrichments in *cis* (blue), *medial* (orange) and *trans*-species (green) during vesicular transport (details of computations of this enrichment presented in App.2, p.26) as a function of k_b .

1359

Linear budding

To verify whether the assumption of saturated budding (Eq.2) has a strong impact on the results, we performed simulations with a linear budding mechanism ($f(\phi) = \phi$ in Eq.10), for which the budding flux for a given identity is linear with the number of patch with this identity ($J_{b,i} = K_b n \phi_i = K_b n_i$). As shown in Fig.1A-B - current appendix, the average compartment size and purity follow the trends discussed in the main text for the saturated budding regime. However, the purity transition occurs for larger k_b , since the total budding flux is merely

1363

Manuscript submitted to eLife

1364

1365

1366

1367

1368

1369

1370

1371

1372

1373

1374

1375

1376

1377

1378

1379

1380

1381

1382

1383

1384

1385

1386

1387

1388

1389

1390

1391

1392

1393

1394

1395

1396

1397

1398

1399

1400

1401

1402

1403

1404

1405

1406

1407

1408

1409

1410

1411

1412

proportional to the size of the compartment for linear budding, and is thus smaller than for saturated budding, where it is proportional to the size times the number of species. Saturated budding thus promotes systems that are at the same time well sorted, and with large compartments.

Even though the purity transition is shifted toward higher values of k_b , the link between purity and vesicular flux is qualitatively conserved (Fig.1C - current appendix). For low purity, the system is retrograde with an enrichment in *cis*-species and a depletion of more mature species, and for high purity it is anterograde. However the retrograde flux is less marked than with a saturated budding rate (no clear depletion in *trans*-species). Indeed, efficient sorting relies on the capacity to export the minority component out of a compartment. Within the saturated budding scheme, the rate of export is proportional to the size of the compartment and does not depend on the number of minority components to export. Within the linear budding scheme however, it is proportional to the number of minority components. In the low k_b regime, *trans*-rich compartments are large. They emit a large vesicular flux of immature components within the saturated budding scheme, but this flux is much smaller within the linear budding scheme. This explains the qualitative difference between the enrichment curves in the low k_b regime for the saturated budding scheme (large depletion in *trans* identity - Fig.3 - main text) and the linear budding scheme (almost no change in *trans* identity - Fig.1C - current appendix).

Non-fusing compartments

Fusion between compartments is an important ingredient of the model discussed in the main text. It could be argued that the fusion of large cisternae with one another could be a much slower process than fusion involving much smaller transport vesicles. We have performed simulations where fusion between compartments is prohibited if both compartments are larger than a vesicle. Note that in the model, such compartments are still able to fuse with the boundaries, so that the composition of the system can still be predicted by Eq. 4. The results of this model are shown in Fig.1D-F - current appendix.

The size distribution of non-fusing compartment shows a broad peak, instead of the power-law seen in the case where compartments can fuse. As compartments can only grow by vesicle fusion and not by compartments fusion, their size is smaller than in the previous case. The compartments size is results from a balance between the rate at which compartments are recycled (fuse with one boundary) and the rate at which they grow by vesicle fusion. Consequently, the size distribution only weakly depends on k_b , as compartments have very little time to fuse with vesicles before exiting the system (Fig.1-D - current appendix).

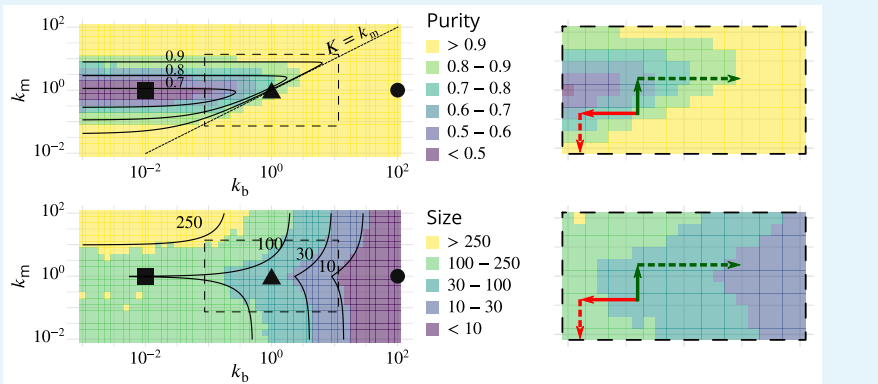
As expected, and because we remove the possible interactions between compartments, the centripetal flux we observe between the previously described anterograde and retrograde is abolished. This is particularly visible if we plot the (normalized) mean enrichment in *cis*, *medial* and *trans*-species seen by cargo as they are transported via vesicular fluxes (Fig.1-F - current appendix). As before, the system goes from a purely retrograde flux, characterized by a depletion in *trans*-species and an enrichment in *cis*-species, to an anterograde flux, characterized by an enrichment in *trans*-species and a depletion in *cis*-species. However, the transitional centripetal regime we previously described, characterized by an enrichment in *medial*-species, vanishes. This suggests this particular regime is indeed resulting from the possible fusion between compartments, as it destabilizes *medial*-compartments that have a great probability to fuse with slightly impure *cis* or *trans*-compartments. Thus the transport is anterograde as soon as the purity transition occurs (Fig.1E - current appendix).

1413 **Appendix 9**

1414

EXPERIMENTAL PROPOSAL

1415



1416

1417

1418

1419

1420

1421

1422

1423

1424

1425

1426

1427

Appendix 9 Figure 1. Possible experimental strategies to test the predicted correlation

between size and purity of Golgi cisternae. The left column reproduces Fig.2B-C, showing the phase diagrams for the purity (top) and size (bottom) of Golgi cisternae upon varying the ratio of budding to fusion rates k_b and the ratio of biochemical conversion to fusion rate k_m . The right column shows a zoom of the dashed square area, showing the observed result of physiological perturbations of cisternae purity and size (solid arrows) and prediction for combined perturbations (dashed arrows). Red arrow: observed result of a decrease of the budding rate k_b by impairing COP I (*Papanikou et al., 2015*). Dashed red arrow: prediction for the combined decrease of the biochemical conversion rate k_m by Ypt1 down-regulation. Green arrow: observed result of an increase of the biochemical conversion rate k_m by Ypt1 over-expression (*Kim et al., 2016*). Dashed green arrow: prediction for the combined increase of the budding rate k_b by COP I up-regulation.